Materials and Design 181 (2019) 108067

Contents lists available at ScienceDirect

Materials and Design

journal homepage: www.elsevier.com/locate/matdes

Topology and mechanics of metal rubber via X-ray tomography

Yanhong Ma [a], Qicheng Zhang [a,b], Yongfeng Wang [a], Jie Hong [a,*], Fabrizio Scarpa [b,*]

[a] School of Energy and Power Engineering, Beihang University (BUAA), Beijing 100191, PR China
[b] Bristol Composites Institute (ACCIS), University of Bristol, University Walk, BS8 1TR Bristol, UK

HIGHLIGHTS

- Metrics are defined to quantitatively describe the internal microstructure of metal rubber
- The transverse isotropy of the wire orientation in metal rubber is observed and quantified
- The mechanical properties are here explained by combining a reduced order helix cell model and the internal structural characteristics
- The effect of different manufacturing parameters on the mechanical properties and microstructures of metal rubber are tested and analyzed
- The metal rubber wire diameter has the largest effect on the structural and mechanical isotropy of this porous material

GRAPHICAL ABSTRACT

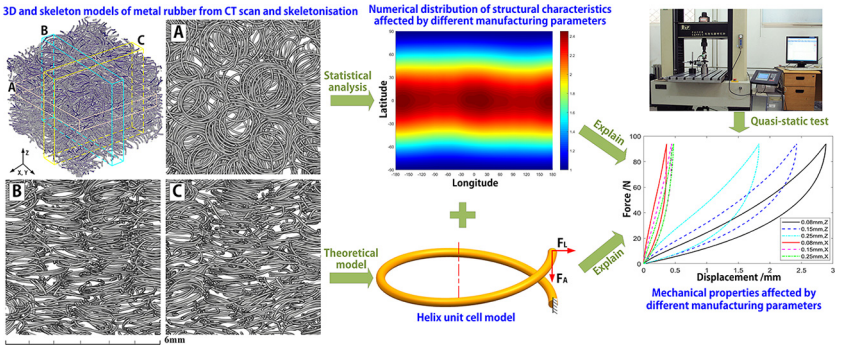

ARTICLE INFO

Article history:
Received 6 May 2019
Received in revised form 14 July 2019
Accepted 22 July 2019
Available online 26 July 2019

Keywords:
Metal rubber
Entangled wire mesh
CT scan
Topology
Microstructure parameters
Mechanical property

ABSTRACT

This paper describes the structural characteristics of metal rubber (MR) evaluated by X-ray tomography and skeletonisation at microscopic scale. The parameters used to describe the internal structure of the MR were numerically extracted and compared to assess the effect of different MR manufacturing parameters on the mechanical properties of the material. Quasi-static tests were also performed to obtain the stiffness and damping of the metal porous material and to understand their correlation with the topology defining the samples. A simplified helix cell model was used to interpret the mechanical properties of the MR based on the structural parameters identified in this paper. The transverse isotropic stiffness of the MR observed here is partly caused by the distribution of the metal wires, with more helices oriented along the molding direction resulting in smaller equivalent stiffness. The compression, relative density, helix and wire diameters can influence the structural and mechanical characteristics of the MR in a significant manner.

1. Introduction

Metal rubber (MR) is a type of porous metal material possessing high stiffness and damping, and made via wire weaving and compression molding. The term metal rubber is coined by the observation that this material behaves similar to an elastomeric rubber in terms of mechanical performance. However, it must also be noted that some researchers prefer to use different terms to define the material, such as entangled metallic wire material (EMWM) [1,2], metal wire mesh [3–5] or pseudo-rubber [6]. Metal rubber is suitable for vibration energy and sound absorption [7–9] in harsh temperature environments (−100 °C to 200 °C [10–12]), heat transfer [13] and also surgical implants and internal prosthesis [14]. As a multifunctional smart material, metal

* Corresponding authors.
E-mail addresses: hongjie@buaa.edu.cn (J. Hong), f.scarpa@bristol.ac.uk (F. Scarpa).

https://doi.org/10.1016/j.matdes.2019.108067

rubber has also been developed in shape memory alloys [6,15–18], magnetostrictive [19,20] and even auxetic versions [21].

The mechanical behavior of the MR is influenced by parameters such as the relative density (i.e., related to the porosity), the wire and helix diameters, and the material properties of the materials constituting the wires. MR samples made of nickel-based superalloy [22–27], aluminum alloy [28] or titanium [29,30] have been previously tested, and the effects of the relative density on the compressive modulus, Poisson's ratio and loss factor were observed. The performance of MRs under uniaxial tensile [31,32] and torsion [33] has been assessed by Liu and Tan et al. Vibration tests have demonstrated that the dynamic properties (storage modulus and loss factor) of metal rubber can also be affected by the frequency and dynamic strain adopted during the tests [15,27,34]. Although a significant body of work has been already performed to characterize the materials, the effect of the helix and wire diameters on the MR mechanical properties is still poorly understood [17,35].

Constitutive models of MR are built based on the use of cantilever beam cells [36] or helix units [37–40]. These models describe the homogenized mechanical behavior and hysteretic loss factors from different perspectives. All these models use assumed unit cells and obtain the parameters of the unit cells by inverse identification from experimental mechanical data. Among all these models, the one characterized by the use of helix units tends to provide better results [40], and can also be used to physically interpret some mechanical properties of the metal rubber. There is however a need to evaluate and relate the structural characteristics and internal topology of this metal porous solid MR with a constitutive model.

Industrial CT (computed tomography) scans are widely used to obtain the internal structure of porous materials. Tan et al. [41] and Masse et al. [42] have extracted the skeleton of sintered steel wools based on X-ray microtomography and by using a three-dimensional skeletonisation algorithm. By using these techniques, they have been able to analyze the fiber orientation, number of contact pairs and distributions of the fiber segment lengths in the metal wools. A similar methodology was used by Wang and Huang [43,44] to study the morphologic characteristics of porous metal fiber sintered sheet. Gadot and Rodney et al. [17,35] obtained the 3D model and centerline of entangled single-wire materials by X-ray tomography, and built the relative finite element model to study the internal structure and its mechanical properties. However, their studies did not consider parameterized effects of material parameters, such as wire and helix diameters. These studies proved though that CT scan and skeletonisation methods work well for fiber shaped porous materials, including MR.

In this paper we have used CT scans and skeletonisation methods to study the structural topologies of metal rubber and their constitutive parameters. Quasi-static mechanical tests have also been performed to investigate relations between the MR parameters and their mechanical properties, and justified by using a combination of the helix cell model and the experimental mechanical results. The first section of the paper describes the MR specimens used in this

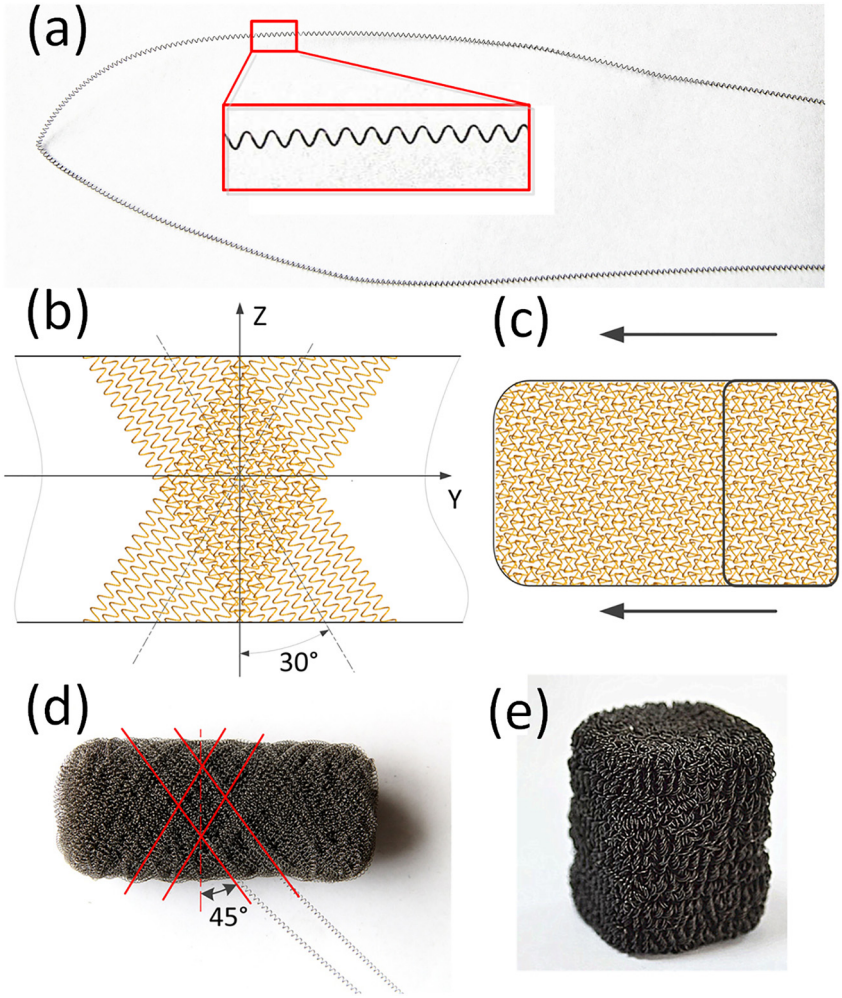

Fig. 1. MR manufacturing process, including helix wire tensioning (a), wire weaving (b) and coiling (c), then crisscross weaving on the out layer (d) and finally the molding (e).

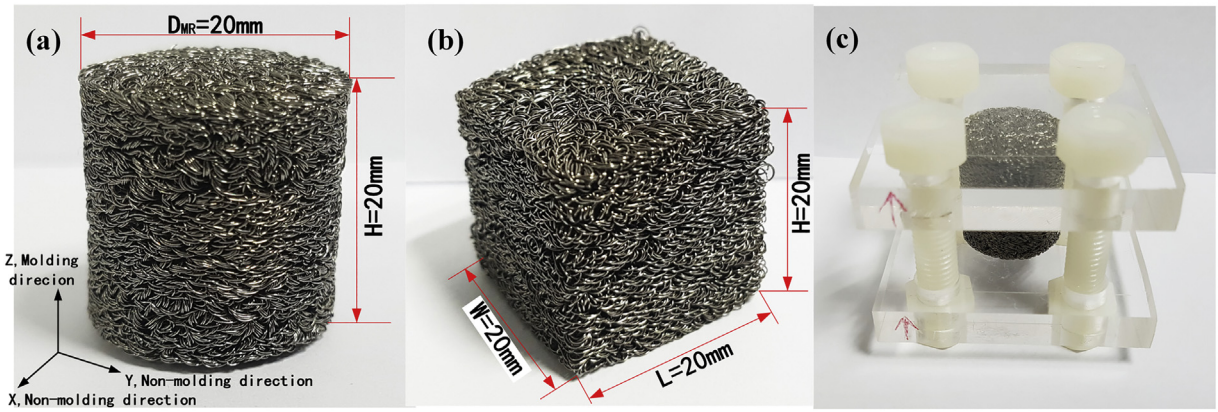

Fig. 2. MR specimens (a) cylinder specimen for CT scan and quasi-static test, (b) cube specimen for quasi-static test in molding and non-molding directions, (c) specimen under compression for CT scan.

Table 1
MR specimens with different manufacturing parameters.

Specimen shape	Specimen number	P_C^a	ρ_r^b	D_H^c/mm	D_W^d/mm
Cylinder	1–1	0	0.17	1.5	0.08
	2-1a	0	0.23	1.5	0.08
	2-1b	0	0.23	1.5	0.08
	2-1c	0	0.23	1.5	0.08
	3–1	0	0.28	1.5	0.08
	4–1	0	0.23	1.0	0.08
	5–1	0	0.23	2.0	0.08
	6–1	0	0.23	1.5	0.15
	7–1	0	0.23	1.5	0.25
	2-1a-2 mm	10%	0.23	1.5	0.08
	2-1a-4 mm	20%	0.23	1.5	0.08
	2-1a-6 mm	30%	0.23	1.5	0.08
Cube	8–1	0	0.23	1.5	0.08
	9–1	0	0.23	1.5	0.15
	10–1	0	0.23	1.5	0.25

work. The second section illustrates the research methodology adopted, including the CT scan and the skeletonisation methods, the quasi-static tests and the simplified helix cell model. Section 4 illustrates the four types of parameters used to describe the microstructure of the MR material. The final sections are related to the elaborations of the relations between topological and structural parameters, and the mechanical performance of the metal rubber. The work in this paper is mainly focused on the quasi-static properties and their relationship with the internal structural configuration of this metallic porous material. The hysteretic behavior of the MR material and its relation with the internal topology of the material can also be evaluated, based on the methods and ideas developed in this paper.

2. MR specimens used in this work

The manufacturing process to produce metal rubber used in this paper is shown in Fig. 1. Nickel-based stainless steel wire with diameter of D_W is first coiled into tight helix shapes with a helix diameter of D_H, by distortion. The wires are then tensioned at both ends to provide an initial pre-tension state with a lead angle α (Fig. 1a). The drawn helix wire is then weaved on a nail board with a crossing angle θ (Fig. 1b). The next step consists of coiling the wire into a cylinder shape (Fig. 1c), and then crisscross weaving the wire on the outer layer to obtain a rough porous base material (Fig. 1d). The sample is finally placed into a specially designed mold and compressed by a force ranging between 10 kN and 60 kN, depending on the parameters of the MR specimens needed, for at least 1 min (Fig. 1e).

One of the MR specimens used for CT scan is shown in Fig. 2(a). The specimen has a cylindrical shape with a diameter of 20 mm and a height of 20 mm. Those dimensions are common to all the cylindrical specimens used in this work. Metal rubber has transverse isotropic properties [15], with different stiffness along the molding and non-molding directions. Three cubic specimens with different

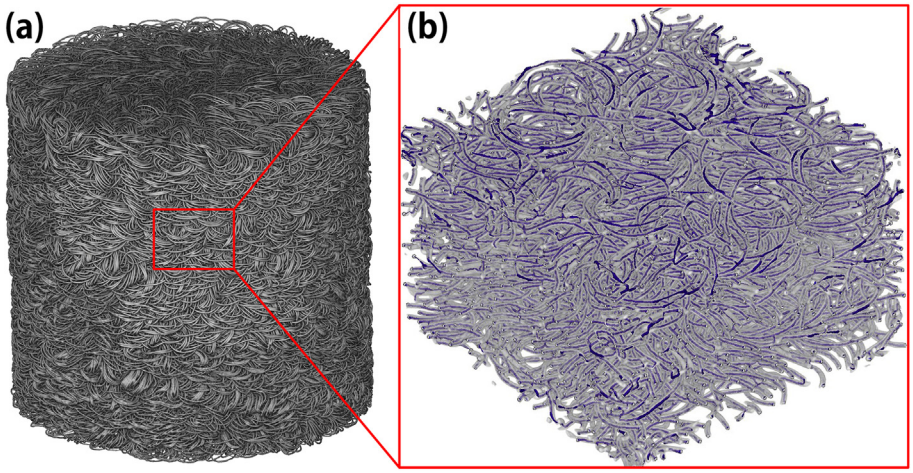

Fig. 3. 3D model of MR specimen (a) and results from the extraction of the skeleton of the MR sample (b).

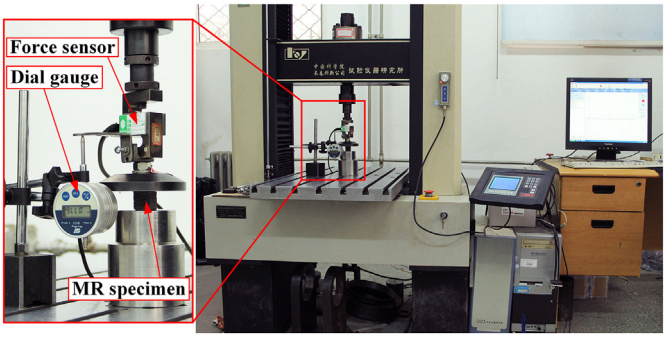

Fig. 4. Quasi-static uniaxial compression rig.

wire diameters have been used for the quasi-static tests to compare the mechanical properties along the molding and non-molding directions (Fig. 2(b)).

A special device was designed to provide different compression strains P_C on the MR specimen during the CT scan(Fig. 2(c)). The MR specimen is clamped between two thick acrylic plates with four nylon bolts providing an adjustable compression. Because the transmissibility of X-rays through acrylic and nylon plastics is significantly higher than in the MR, the effect of the clamping device on the scanning results can be considered negligible.

The manufacturing parameters in the manufacturing process shown in Fig. 1 (relative density ρ_r, wire diameter D_W, helix diameter D_H, weaving crossing angle θ, ratio of specimen height over coiled cylinder-shaped base material height ζ_h,) can affect the properties of the MR in some degree. Based on empirical experience, the weave crossing angle and the ζ_h parameter are usually set *at* 30° at 3 respectively, to obtain a stable and consistent MR specimen. Thus, only the effect of ρ_r, D_W and D_H are investigated in this paper. The relative density ρ_r of the MR material is here defined as the ratio between the metal rubber mass to its volume, times the density of the Nitinol based stainless steel material (7900 kg/m^3).

The parameters of different MR specimens used in this work are listed in Table.1 (13 cylindrical and 3 cubic specimens). Among them, #2-1a, #2-1b and #2-1c have same parameters, which are used to study the structural deviation of different MR specimens with same parameters. #2-1a, #2-1a-2 mm, #2-1a-4 mm and #2-1a-6 mm are the same MR specimen clamped in the device of Fig. 2(c), having 0 mm, 2 mm, 4 mm and 6 mm compression deformation respectively, with P_C = 0%, 10%, 20% and 30%. The effects of the relative density ρ_r, the wire diameter D_W and the helix diameter D_H are evaluated in the different specimens described in Table.1.

3. Methodology

3.1. CT scan test and 3D model skeletonisation

Computed tomography (CT) on the metal rubber was performed using a Nikon XT H 225 Industrial CT Scanning machine. The voxel

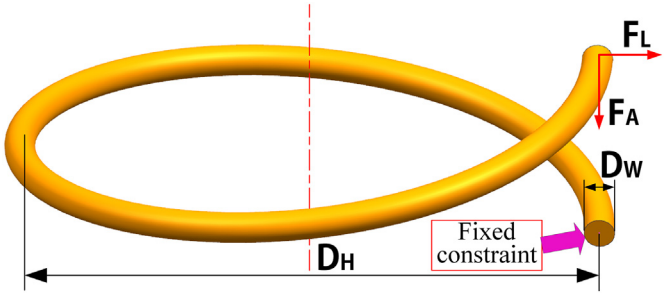

Fig. 5. Scheme of helix unit cell model.

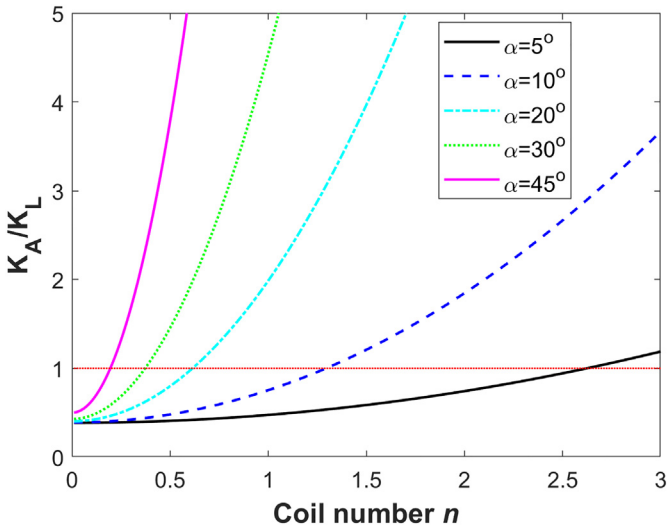

Fig. 6. The ratio of K_A/K_L versus coil number n.

resolution of the CT scanning is 0.015 mm, which is a sufficiently small value for the MR specimen with the smallest D_W diameter of 0.08 mm.

The 3D model of the MR specimen (Fig. 3(a)) was generated from the CT data using the Avizo 9.0 software (developed by FEI Company). From an initial visual inspection of the 3D image, it is possible to evince the presence of a high interconnectivity existing between the tangled wires and the global topological feature of the porous structure.

The 3D model only provides a visible impression of the internal microstructure of the MR. A more quantitative information is provided by the definition of its skeleton, which was built by extracting the centerlines of the MR wires using the custom module presented in Avizo 9.0. The skeleton model and the 3D model of the MR cuboid sample are shown together in Fig. 3(b). It can be seen that the skeleton model overlaps with the 3D model well and can be used to describe the topological characteristics of the metal rubber. The skeleton model is composed of nodes and segments, processable in MATLAB. Thus, the statistical result of MR topological characteristics can be defined and obtained based on the skeleton model.

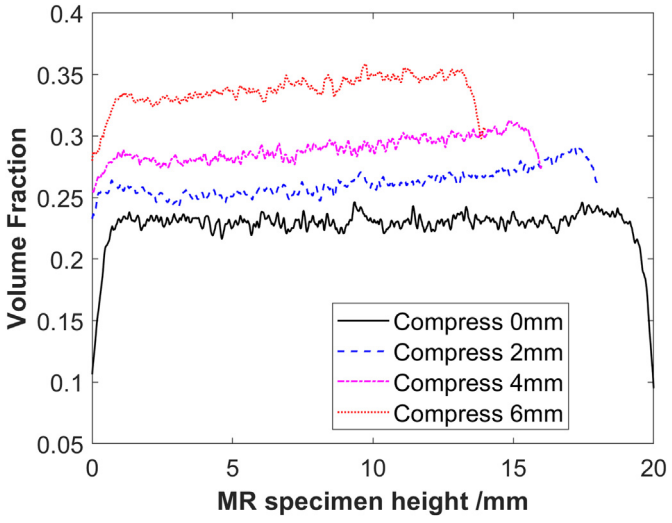

Fig. 7. Wire fraction versus specimen height of the MR samples under different compressions.

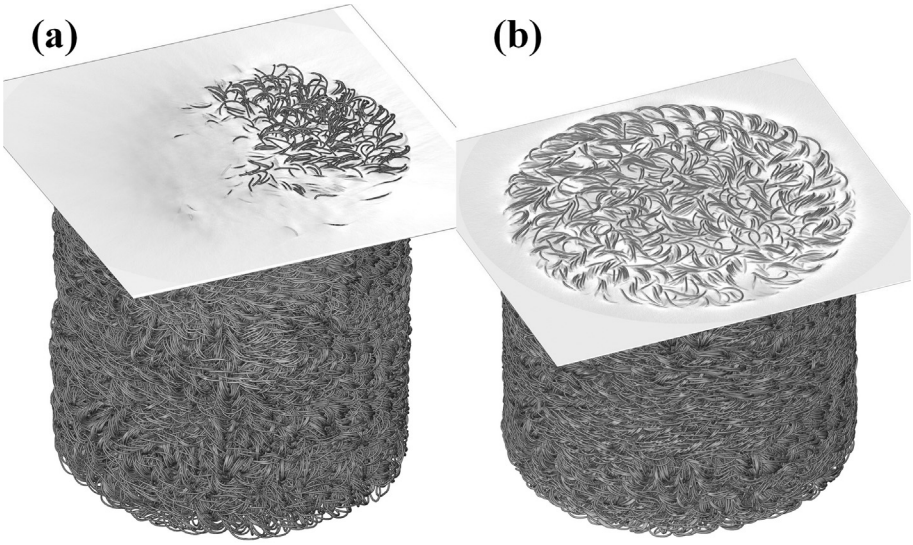

Fig. 8. Boundaries of a MR sample under different compression strains (a) $P_C = 0$, (b) $P_C = 30\%$.

3.2. Quasi-static test rig

Quasi-static uniaxial tests were performed using the test rig shown in Fig. 4. The tests were carried out using a WDW 3100 electronic universal testing machine with a 1.0 kN force sensor and a 25 mm electronic dial gage for the deformation measurements. The tests were performed under displacement control, with loading and unloading rates of 0.25 mm/min and 0.5 mm/min respectively. An initial preload of 5 N was applied on all specimens to reduce the influence of the uneven contact between the MR specimen and loading plate at small deformations [23].

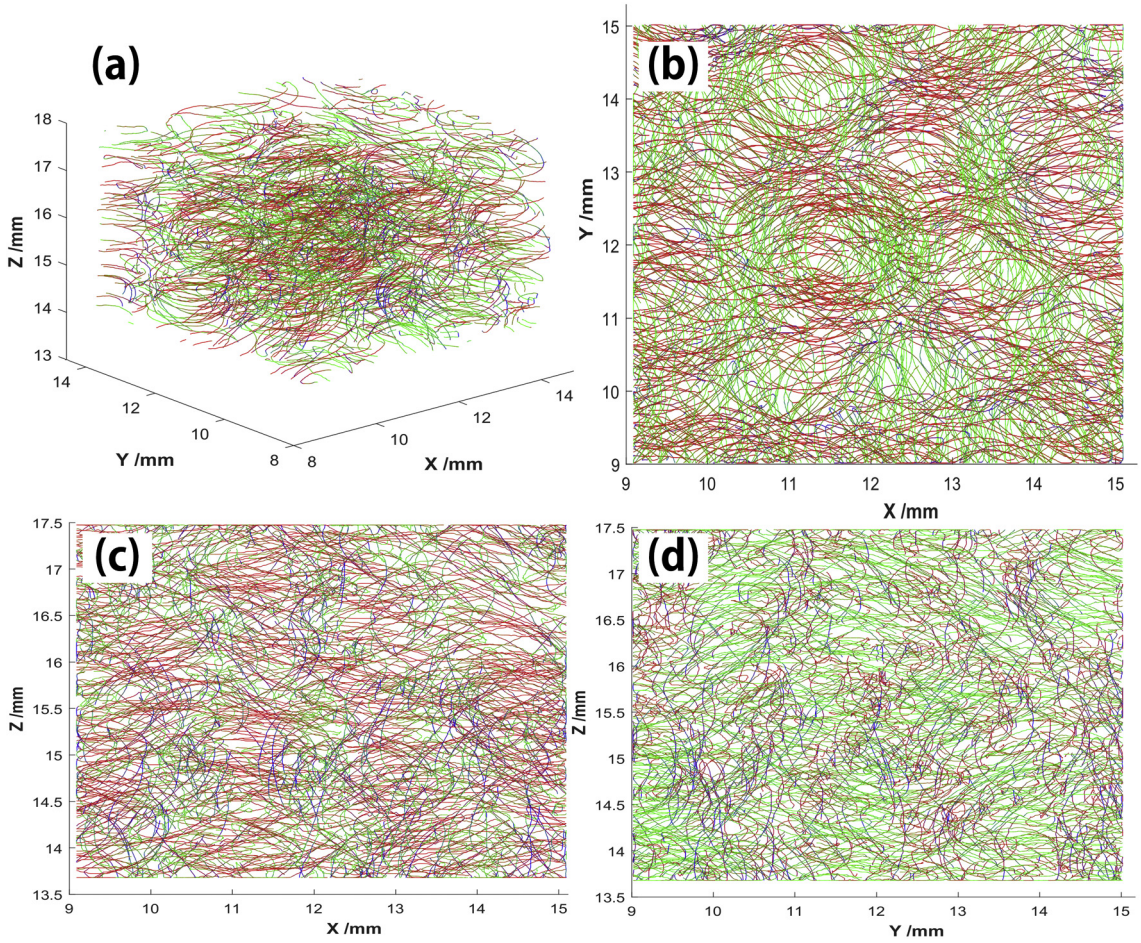

Fig. 9. Dyed skeleton of the #1–1 MR (red in X direction, green in Y direction, blue in Z direction). (For interpretation of the references to color in this figure legend, the reader is referred to the web version of this article.)

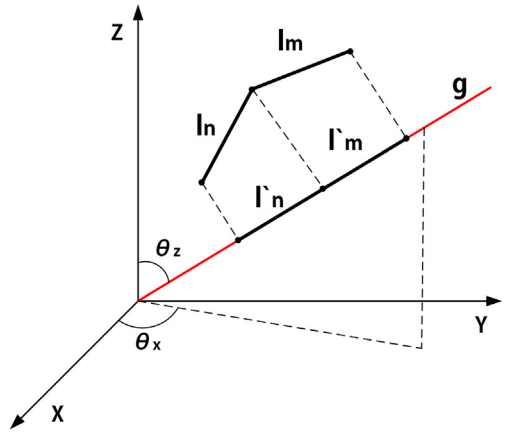

Fig. 10. Illustration of wire segments projecting along the g vector.

3.3. Helix cell model

The manufacturing procedure affects the internal structure of the helix wire-based MR material. Therefore, the helix cell model was used to describe the effect of different topological parameters of the porous solid on the global stiffness (Fig. 5). The helix cell is composed of a single coil fixed on one end of the wire and loaded on the other end by the F_A and F_L forces along the axial and radial directions. As it will be apparent from the CT scans, the number of effective coils in the MR material is small because the wire is separated into small segments by several contact pairs. It should be noticed that the wires in the metal rubber are continuous, and the contact pairs only serve as constraints added to the wires. However, the length and distribution of the free wire segments between two contact pairs are essential for the stiffness of MR. Thus, the lengths of the wire segments can be described as the coil number n and used in following expression (1). The resulting axial and lateral stiffness of the helix can be therefore expressed in Eq. (1) when the ratio of D_H/D_W is higher than 5 [15].

$$K_A = \frac{ED_W\cos\alpha}{16n\left(\frac{D_H}{D_W}\right)^3(1+\nu\cos^2\alpha)}$$
$$K_L = \frac{ED_W\cos\alpha}{8n\left(\frac{D_H}{D_W}\right)^3\left[\frac{4(2+\nu)n^2\pi^2+3\nu/2}{3}\tan^2\alpha+1\right]} \quad (1)$$

In (1), K_A and K_L represent the axial and lateral stiffness of helix respectively. The Young's modulus of the wire material is E and ν is the Poisson's ratio. The angle of the helix is α, and n is the number of the coil.

From inspection of Eq. (1) one can notice that K_A and K_L both increase monotonically with D_W and decrease with D_H and n. The curves of K_A/K_L ratio versus the number of coils n with different lead angles α are shown in Fig. 6. The K_A/K_L ratio rises monotonically with n from ~0.4 to values larger than 1. This implies that the axial stiffness K_A is smaller than the lateral one K_L for helix topologies with small n, and it is on the contrary larger in helix systems with big n values. The ratio K_A/K_L also increases significantly with α, so that the value of n for $K_A = K_L$ is reduced significantly. The helix cells in MR materials mostly possess angles $\alpha < 10°$ and $n < 0.5$, as it will be shown later. Those results indicate that the axial stiffness of coils in manufactured metal rubber materials is typically lower than the lateral one.

4. Parameters used to describe the microscopic internal structure of metal rubber

Different statistical parameters have been defined to describe the MR internal structure. Those include the fraction of wires at each section (slice) of the specimen, the distribution of the orientation of the wires, the density of the contact pairs and the quantity of wire segments with different lengths.

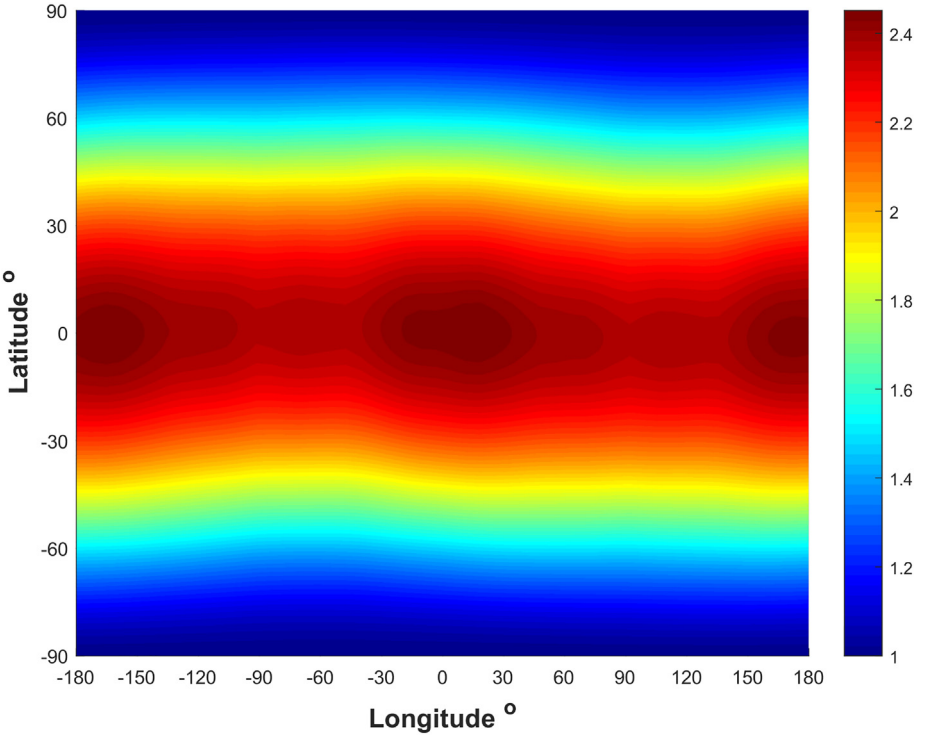

Fig. 11. Orientation distribution map of the wires in the #2-1a sample.

4.1. Fraction of wire at each section

The cross section of MR specimen is obtained from a plane cutting the specimen parallel to the top and bottom surfaces, which can be seen in Fig. 12(A). The fraction p_n of wires at the nth section is defined as follows:

$$p_n = \frac{A_{wire-n}}{A_{all-n}} \tag{2}$$

In (2) $A_{wire\text{-}in}$ represents the area of the steel wire at the nth section and A_{all-n} is the area of the specimen cross section, which equals to $\pi D_{MR}^2/4$, with $D_{MR} = 20$ mm being the specimen diameter.

The fractions of the wires at different cross sections of the specimen are shown in Fig. 7. The p_n values in the central parts of the MR specimen are constant for a specific height, and this corresponds to the MR relative density. The curves however drop significantly at the bottom and top boundaries, with less wires there. This has been defined as the boundary layer effect, and affects the overall mechanical property of metal rubber samples significantly [25].

When compressive deformations are applied, the thickness of the boundary layer decreases and the wire fraction reduction is lower (Fig. 7). The boundary layer effect in MR materials is mainly due to the unevenness of top and bottom surfaces and the outstretched helix at the two surfaces. When the MR specimen is unloaded, the top and bottom surfaces are not flat because of the roughness of the material (Fig. 8(a)). The two surfaces will then become flat under an external compression force (Fig. 8(b)). However, the helix wires stretch out from the surface and make the distribution of wires sparser at the boundary layers compared to the middle section of the specimens.

4.2. The orientation of the wire

To visualize and quantify the orientations of the helix wires, the skeleton model was first subjected to a RGB colormap based on the wires orientation angles. The skeleton model is composed of short line segments. The color of each segment is described by a RGB color model, array of three numbers ranging from 0 to 1:

$$\mathbf{C}_{RGB-n} = \left[c_{r-n}, c_{g-n}, c_{b-n}\right] \tag{3}$$

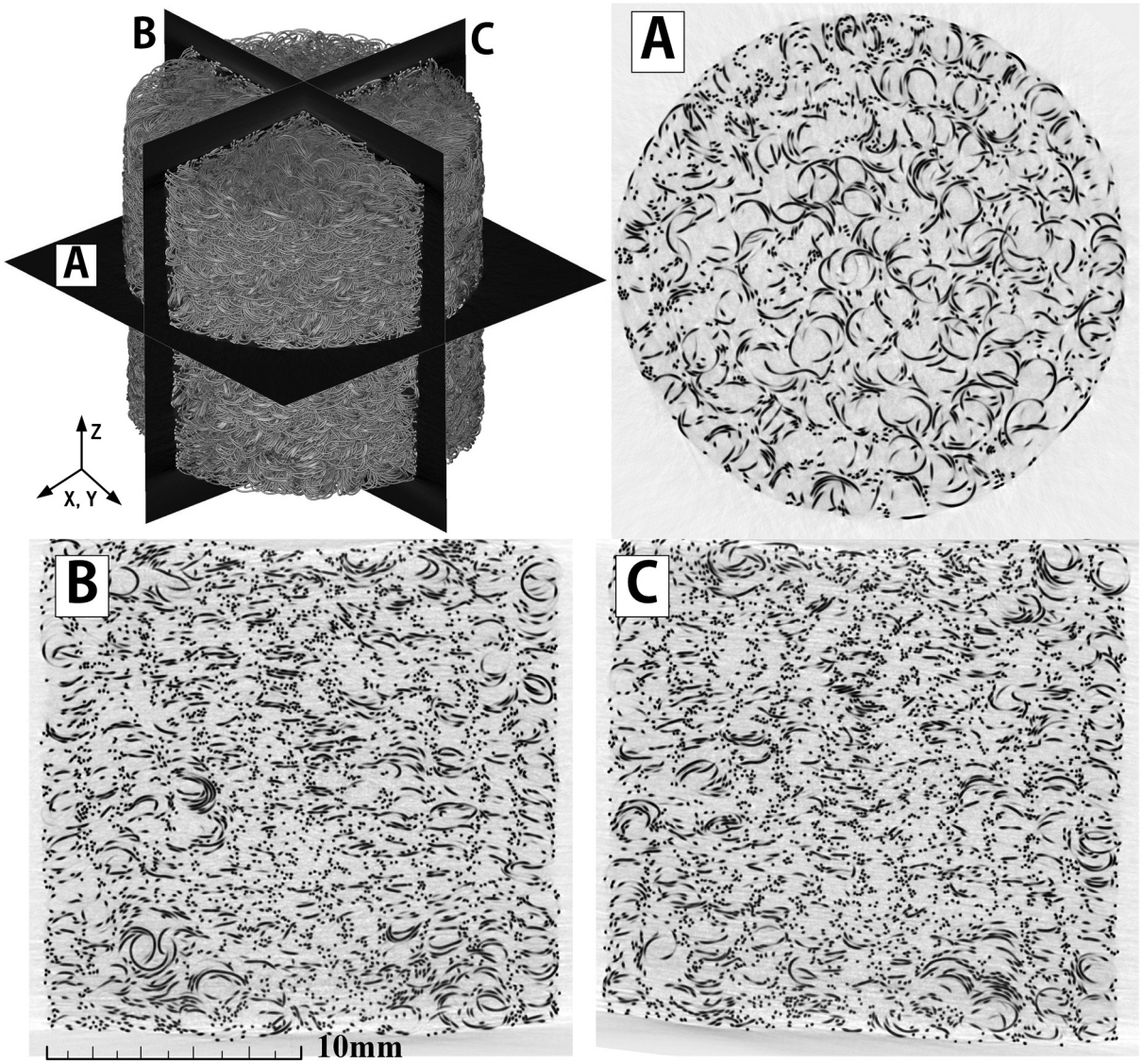

Fig. 12. Section figures of #1–1 MR specimen.

In Eq. (3) the three numbers represent red, green and blue. The RGB array of the *n*th line segment in skeleton model is calculated as:

$$\begin{aligned} c_{r-n} &= \cos^2\alpha_n \\ c_{g-n} &= \cos^2\beta_n \\ c_{b-n} &= \cos^2\gamma_n \end{aligned} \tag{4}$$

In expression (4) α_n, β_n and γ_n represent the spatial angles between the segment line and the global X, Y, Z Cartesian axes. The wire segment is therefore oriented along the axis if its color is similar to three additive primary colors. The Z direction corresponds to molding compression direction.

The dyed skeleton model of a cuboid from the #1–1 MR specimen is shown in Fig. 9. One can observe that the skeleton mainly exhibits red and green colors representing wires along the X and Y directions, while blue is almost non present. This indicates that the wires in a metal rubber sample tend to be essentially distributed along the non-molding directions.

However, the dyed skeleton only provides an incomplete understanding of the orientation of the wires. We have therefore defined a wires orientation distribution map for quantitative analysis in the following manner. At first, all the line segments in the MR skeleton model have been projected along a vector **g** with spatial angles θ_x and θ_z, (Fig. 10).

The sum of all projected line segments l_n along **g** is expressed as:

$$S_g = \sum_{n=1}^{N} \left| l_n \right| \tag{5}$$

The scalar S_g in Eq. (5) represents the projection of all the wires in the MR cuboid sample along a specific spatial direction. By changing the orientation of the vector **g** one could obtain the projections along all spatial directions. The projection S_g was normalized as:

$$q_g = \frac{S_g}{S_z} \tag{6}$$

In Eq. (6), S_z represents the projection along the Z (molding) direction. The normalized projection q_g could then be used to plot the orientation distribution map of the MR wires. Moreover, the ratios r_{yx} and r_{zx} of the projections along the Y and X, and Z and X directions are defined as:

$$r_{yx} = \frac{S_y}{S_x}; \qquad r_{zx} = \frac{S_z}{S_x} \tag{7}$$

These two parameters could be used to perform a comparison of the topologies of the MR samples with different manufacturing parameters.

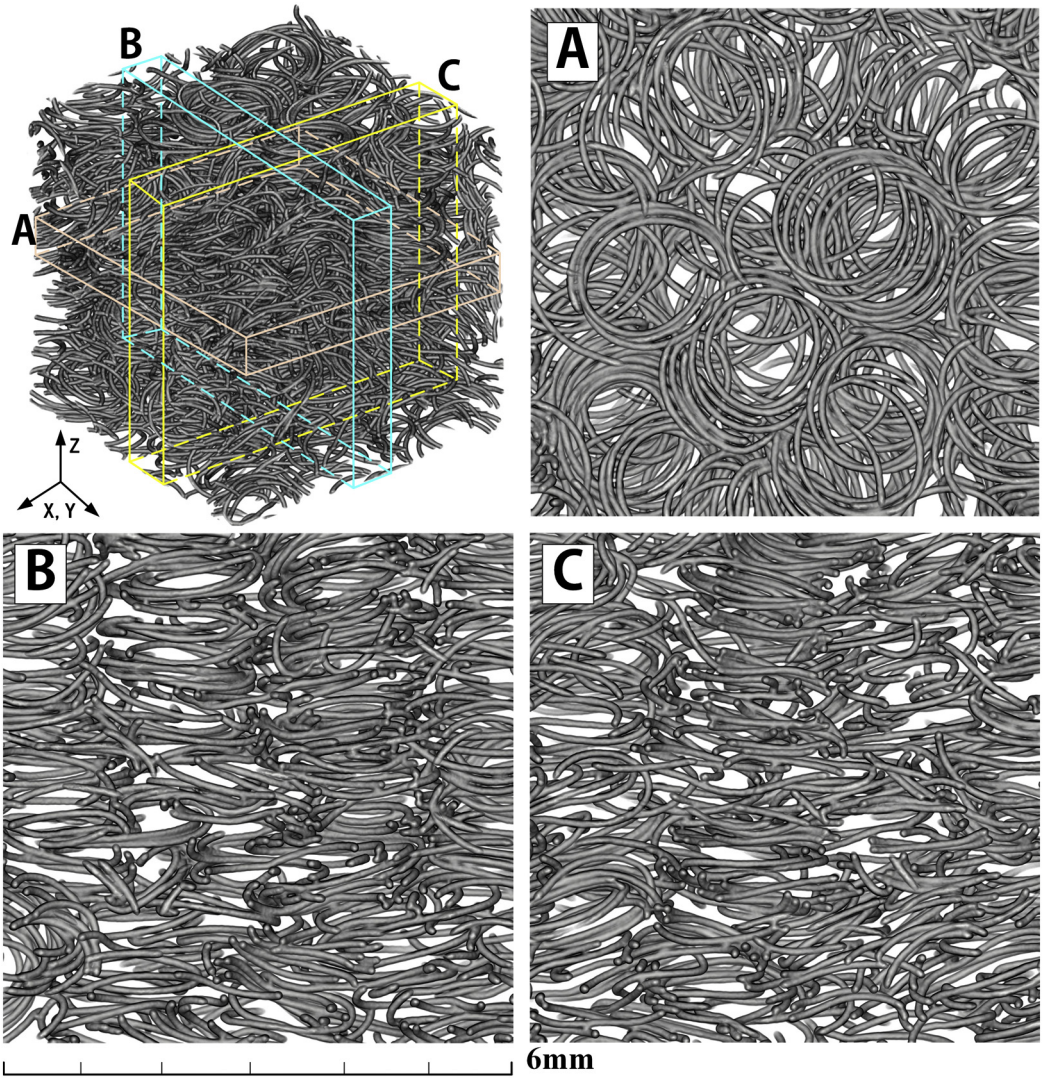

Fig. 13. Slices extracted from the #1–1 MR specimen.

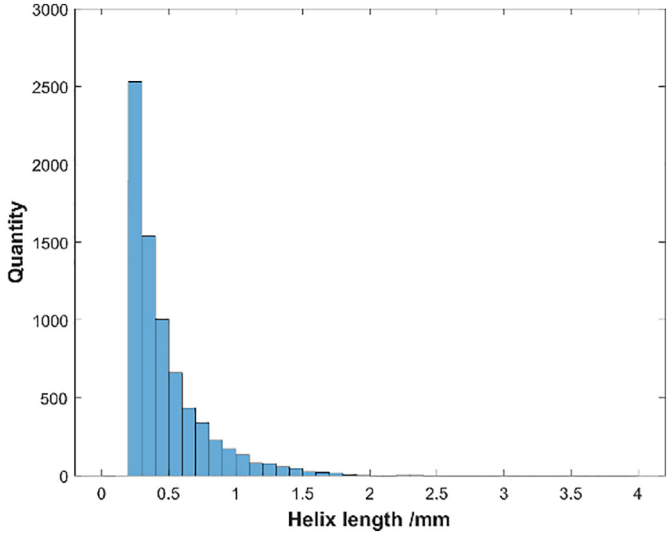

Fig. 14. Distribution of the wire segments with different lengths in the #1–1 MR specimen.

The map describing the distribution of the orientations of the wires in sample #2-1a is shown in Fig. 11. The X coordinate represents the longitude, ranging from −180° to 180°, while the Y coordinate is the latitude (between −90° and 90°). The value of each point on the map represents the normalized projection q_g on the vector with the spatial angle determined by the longitude and latitude of the specific point. From the observation of Fig. 11 it is evident that the normalized projections have the highest values close to the equator and decrease with increasing latitude until reaching a minimum at the two poles. The normalized projection q_g is almost constant for varying longitudes, and this clearly indicates the presence of a transverse isotropy, because more MR wires are distributed in the non-molding plane compared to the other transverse planes. The value of q_g near the equator is around 2.4.

Three orthogonal sections of #1–1 MR specimen are shown in Fig. 12. The black points and rings in the section figure represent the cutting surfaces of the steel wires. A point-shaped cut area indicates that the cutting plane is vertical to the wire axis, i.e. the section is parallel to the axis of the helix. A ring-shaped cut area is indicative of a cutting plane being mainly parallel to the wire ring (section vertical to the helix axis). There is a considerable number of rings present in the A cross section than in the lateral sections B and C. Therefore, the helix cells appear mainly oriented along the molding direction.

Fig. 13 shows three orthogonal slices of the cube sample from the #1–1 MR specimen. The size of the cube sample is 6 × 6 × 6 mm and the thickness of the slice is 1 mm. It is possible to evince from Fig. 13 the significant transverse isotropy of the MR internal structure. The slice A contains a large number of wire rings, while the slices B and C contain only the lateral parts of wire helices, and no obvious difference between the slices B and C can be observed. This is an indication that the axes of helices are mainly parallel along the molding direction, which agrees with the comments drawn from the observation of Fig. 12.

4.3. The density of the contact pairs

The high damping property of metal rubber is mainly caused by the friction at contact pairs between the wires. The contact pairs also subdivide the wires into small parts, and this significantly affects the stiffness of the MR material. Thus, the number of contact pairs per volume (i.e., the density of contact pairs) is defined as:

$$n_{pV} = \frac{n_c}{V} \tag{8}$$

The V in Eq. (8) is the volume of the MR sample, and n_c is the number of contact pairs. The skeleton model of the metal rubber is built by extracting the centerlines from the 3D model. That means the contact pair between wires is merged together as a joint point of adjacent wires in the skeleton model. Thus, the contact points are shared by more than two adjacent segments, which can be detected and counted automatically by the MATLAB codes wrote by the authors. However, the contact state (i.e., stick and slip) cannot therefore be simulated in the skeleton model.

4.4. Distribution of wire segments with different lengths

The contact pairs serve as constraints added on the continuous wires in MR and subdivide the wires into small connected wire segments. A histogram describing the distribution of wire segments with different lengths in the #1–1 MR specimen can be obtained and shown in Fig. 14. The wire segment is defined as the wire between two contact pairs. The segment is not necessarily a straight line, and it may be represented by a curve. The number of wire segments

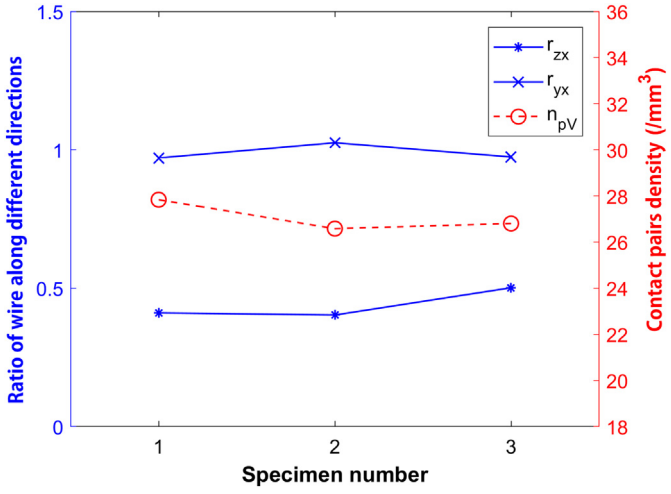

Fig. 15. Wire orientation ratios and density of the contact pairs versus the specimen number.

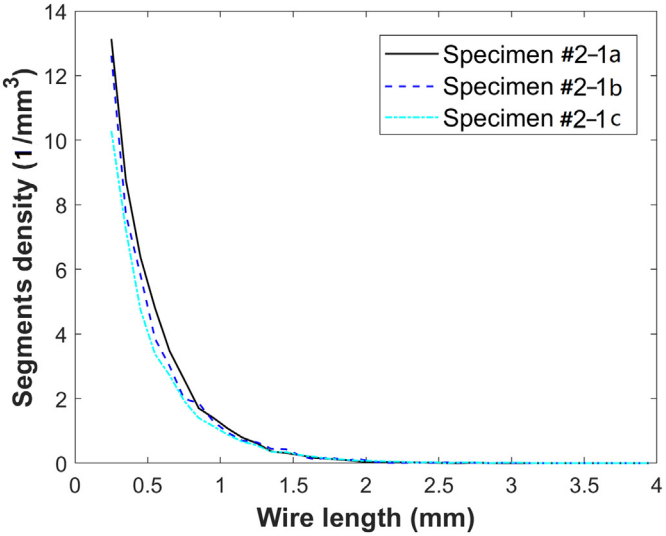

Fig. 16. Segments densities versus segments lengths in different MR specimens.

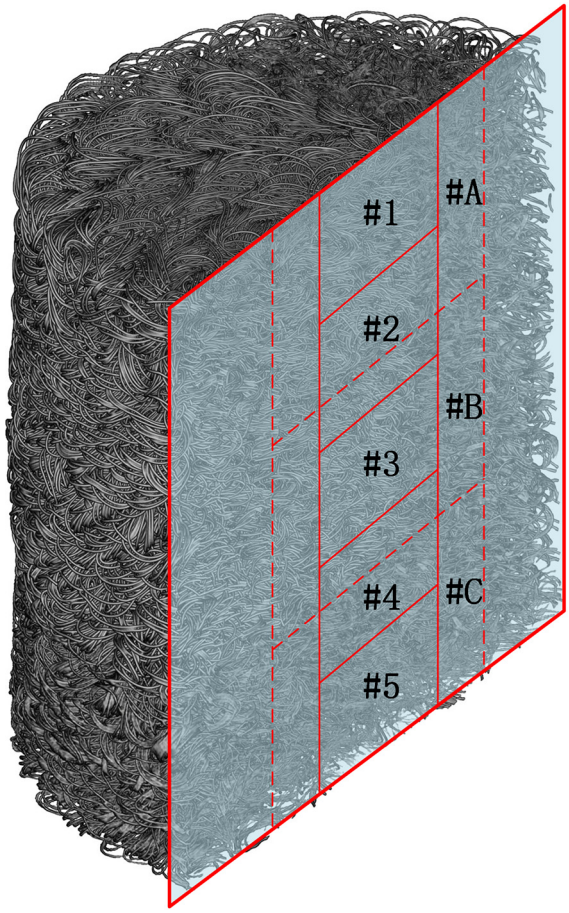

Fig. 17. Cuboids extracted along the height of a MR specimen.

decreases significantly with increasing associated lengths, with the segments mainly ranging between 0.2 mm and 2 mm. This implies that the coil number n of the helix cell model in Fig. 5 is lower than 0.5. The number of wire segments within each length range was divided by the volume of MR sample to obtain the density distribution of segments with different lengths, which was used as metrics to compare the different MR specimens.

5. Uncertainty characteristics of the metal rubber internal structure

5.1. Deviation of different MR specimens with same parameter

The MR specimens #2-1a, #2-1b and #2-1c of Table.1 all possess the same manufacturing and material parameters. The curves describing the wire orientation ratios and the contact pairs density for these three specimens are shown in Fig. 15. The three curves here appear not to offer an obvious dependence versus the number of metal rubber specimen. The r_{yx} ranges from 0.97 to 1.03, which indicates that the length of the wires orientated along different directions in the non-molding plane is quite similar. The metrics r_{zx} ranges from 0.40 to 0.50, denoting a lower portion of wires orientated along the molding direction compared with the non-molding one. Besides, the density of the contact pairs n_{pv} ranges from 26.6 1/mm^3 to 27.8 1/mm^3, with small discrepancies between the different MR specimens.

The curves describing the segments density versus the segment length of the three MR specimens with same parameters are compared in Fig. 16. Also in this case the three curves agree with each other quite well, with segment densities of 1.07 1/mm^3, 0.95 1/mm^3 and 0.88 1/mm^3 respectively within the 1.0–1.1 mm length range. Those values indicate the presence of small deviations between the different MR specimens when the segments density is taken into account.

Besides, the distribution of the wire fractions per section versus the specimen height is quite similar for the three MR specimens having the same parameters. All those samples show similar boundary layers and uniform internal parts (see the black curve of Fig. 7).

5.2. Deviation along the specimen height

Five different cuboid samples were cut out from the MR 3D model along the height (Fig. 17). The dimensions of those cuboids are 6 mm × 6mm × 4mm for free MRs (the total height of the specimen has been divided by 5). The height can be different for MRs with different compression strains. The specimen #7–1 with wire diameter of 0.25 mm has the wires inside too sparsely distributed, so the size of the cuboid must be larger to obtain a sample with a uniform internal structure. Thus, the #7–1 specimen only provides three cuboid samples along height with dimensions 10 mm × 10 mm × 6.6 mm (Fig. 17).

The distributions of the wire orientation ratios r_{yx} and r_{zx}, for the different MR specimens versus the cuboid number are shown in Fig. 18. The curves are almost horizontal, with small deviations among the different cuboids. The values of the r_{yx} parameters are clustered around 1

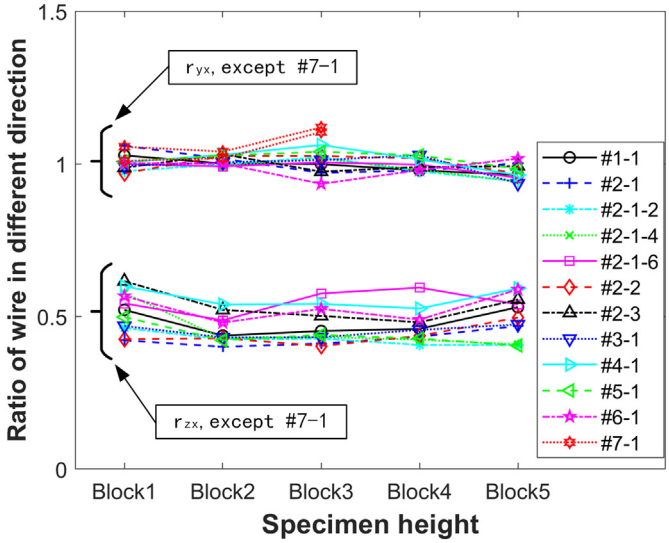

Fig. 18. Wire orientation ratios r_{yx} and r_{zx} versus the cuboid number.

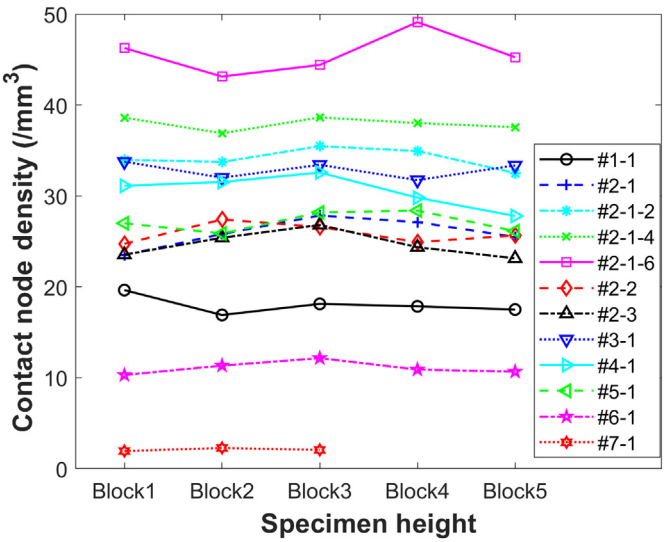

Fig. 19. Contact pairs density n_{pv} versus the cuboid number.

for all the samples considered, while the r_{zx} ratio for all the specimens is close to 0.5, except for the #7–1 sample. It is evident that the transverse isotropy of the MR internal structure is dominant for the different types of MRs except for the material with thick wire, which will be discussed later.

Fig. 19 shows the curves of the contact pairs density n_{pV} versus the cuboid number. Also in this case, the distribution of the contact pairs is predominantly constant along the height. It must be however pointed out that the contact pairs density differs significantly among the various MR specimens, and this will be discussed in the next sections. Besides, the segments density curves of different cuboids belonging to the same MR specimen almost overlap with each other exactly. In that sense the distribution of the curves is similar to the one shown in Fig. 16, so it will not be shown here.

6. The effect of the different parameters

6.1. Variation of compression strain

MR is operationally always used under compression. The specimen #2-1a was scanned under 0%, 10%, 20% and 30% compressive deformations to evaluate the effect of the compression on the MR internal structure. The lateral slices of the MR specimens (sizes 6 mm × 6 mm × 1 mm) with different compression strains P_C are shown in Fig. 20.

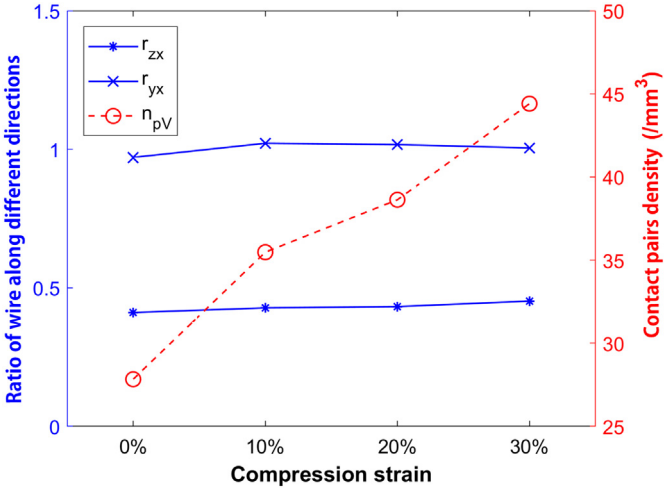

Fig. 21. Wire orientation ratios and contact pairs density versus compression.

The wires appear to become denser with increasing values of P_C, and this is caused by the smaller specimen volume under the external compression.

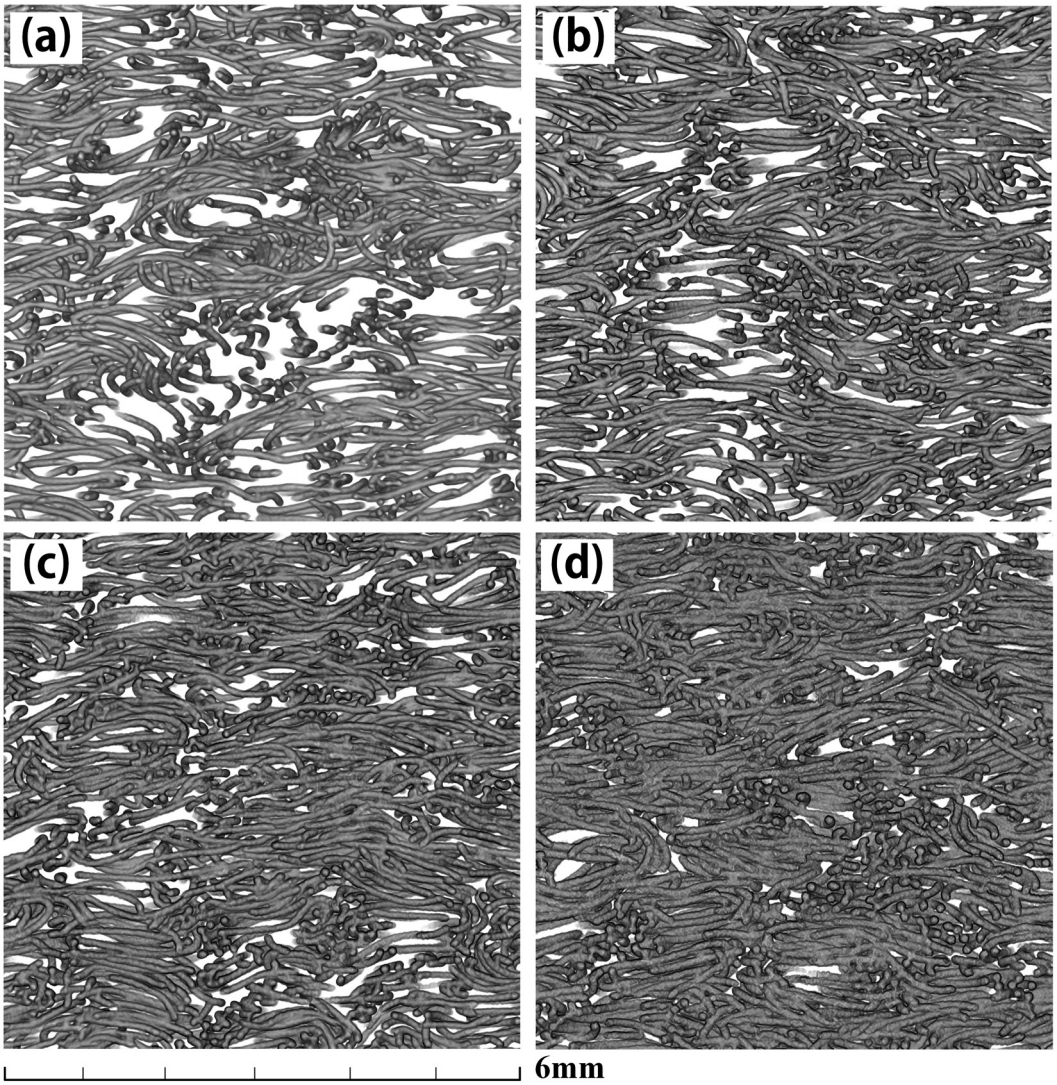

Fig. 20. Lateral slices of MR specimens with different compressions. (a) P_C = 0%, (b) 10%, (c) 20%, 30%.

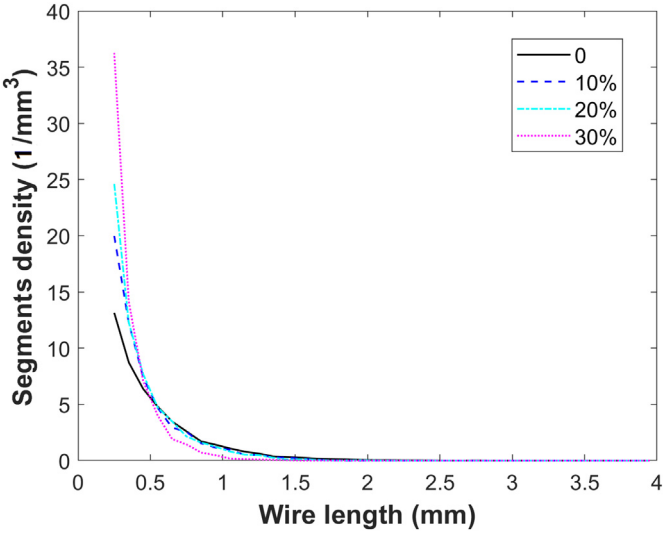

Fig. 22. Segments densities versus segments lengths in MR samples with different compressions.

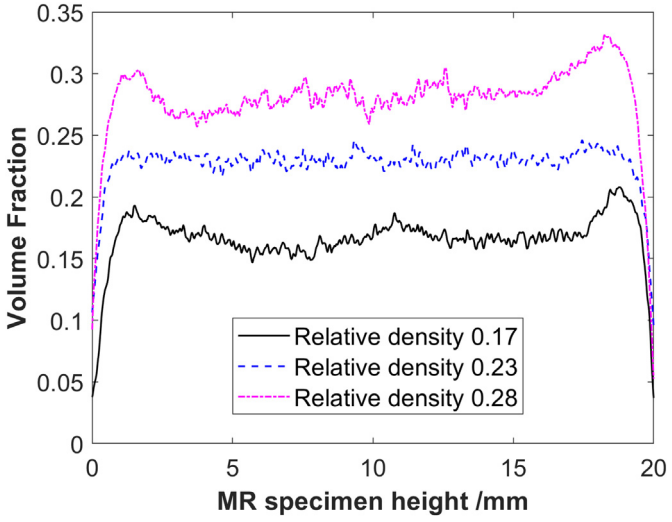

Fig. 24. Section wire fraction versus specimen height of MRs with different relative densities.

The wire orientation ratios and contact pairs densities versus the compressive strains P_C are shown in Fig. 21. The ratios r_{yx} and r_{zx} are almost unchanged for the different P_C values, with r_{yx} ranging between 0.97 and 1.02 and r_{zx} from 0.41 to 0.45. That means the wire orientation inside the MR specimens does not change in an obvious manner with the compression deformation. However, the contact pairs density n_{pV} increases almost linearly with the compression, from 27.8 1/mm^3 at free state to 44.4 1/m^3 for $P_C = 30\%$, a remarkable 59% increase. This can be explained by assuming that the metal rubber becomes much denser under compression (see also Fig. 20). Many wires that were close to contact in the free state would now connect when the external compression is applied, and that results in more contact pairs between the wires.

The segments densities versus segments lengths of the four MRs under different compressions are shown in Fig. 22. The four curves all show a significant decrease trend with the segment length. The curve becomes steeper at low segment length ranges when under larger compressions, with a decreasing number of long segments. For example, the segments densities are 13.1 1/mm^3 and 1.41 1/mm^3 at 0.2 mm–0.3 mm and 0.9–1.0 mm ranges respectively for MR with $P_C = 0\%$. Those values are different from the ones of metal rubber subjected to $P_C = 30\%$ (36.2/mm^3 and 0.47/mm^3 for the same segment lengths ranges). That is because more contact pairs are generated by applying the external compression, therefore the wires are subdivided into more segments. Consequently, the number of short segments increases compared with the reduction of the long ones, and the average length of the wire segments in the metal rubber decreases.

6.2. Variation of the relative density

The relative density ρ_r (related to porosity) is a very important material parameter for porous materials. Therefore, specimens #1–1, #2-1a and #3–1 with nominal ρ_r of 0.17, 0.23 and 0.28 respectively were tested and analyzed to study the effect of the relative density on the MR structural and mechanical characteristics.

The lateral sections of the three MR specimens are shown in Fig. 23. The effective cross sections of the wires obviously increase with ρ_r and the internal structure becomes significantly denser. The percentage of point shaped and ring shaped wire sections do not change significantly across the different slices, indicating a stable wire orientation notwithstanding the value of the relative density.

The distributions of the wire fractions versus the specimen height of the three MRs with different ρ_r values are compared in Fig. 24. The shapes of the three curves are quite similar, with evident boundary layers and relatively flat middle parts. The wire fractions of the cross sections in the middle parts are approximately equal to 0.17, 0.23 and 0.28; these are the same values of the relative densities of each specimen.

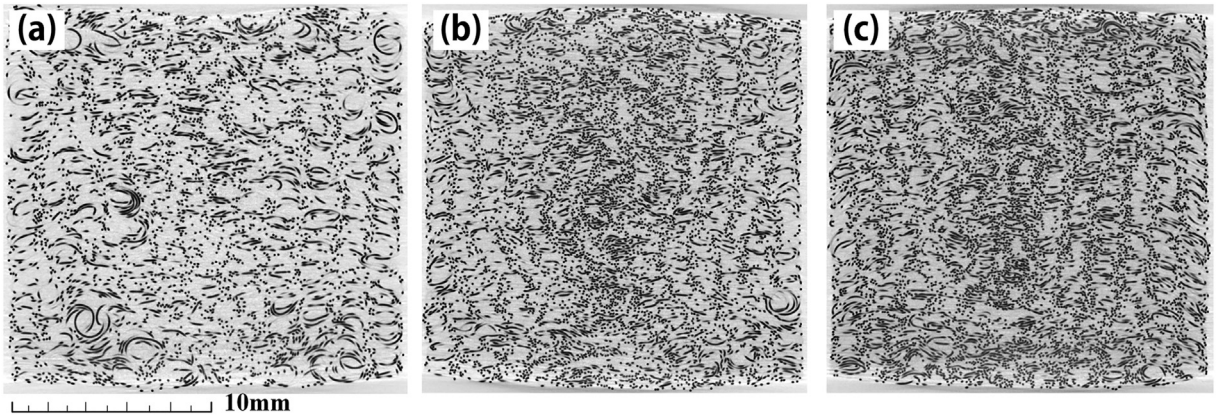

Fig. 23. Lateral sections of the MR specimens with different relative densities. (a) $\rho_r = 0.17$, (b) $\rho_r = 0.23$, (c) $\rho_r = 0.28$.

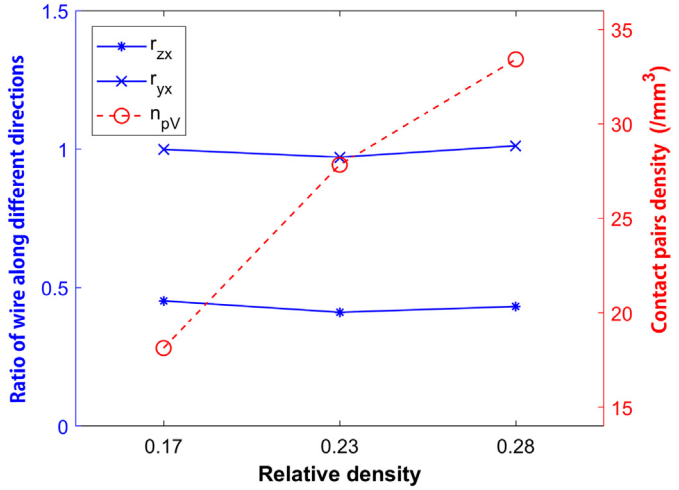

Fig. 25. Wire orientation ratios and contact pairs density versus the relative density.

The wire orientation ratios and the contact pairs density versus ρ_r are shown in Fig. 25. The ratios r_{yx}, and r_{zx} are not noticeably sensitive to the increasing relative density (all ranging between 0.45 and 1). The contact pairs density however almost linearly increases with ρ_r. The effect of the relative density is similar to the one provided by the compression strain, which does not change the wire orientation but tends to increase the contact pairs density. This is due to the fact that the compression deformation reduces the specimen volume, thus increasing ρ_r.

The segment densities versus lengths of the three MRs with different ρ_r are compared in Fig. 26. The three curves show similar trends, with steeper decline for the metal rubber with the highest ρ_r value. For example, the segments densities are 5.2 1/mm^3 and 0.4 1/mm^3 within the 0.2–0.3 mm and 1.5–1.6 mm ranges for MR samples with $\rho_r = 0.17$. Those values are changed to 16.5 1/mm^3 and 0.2 1/mm^3 respectively for the MR material with $\rho_r = 0.28$. The number of short segments increases significantly when the relative density increases, and this is accompanied by a slight reduction of the portion of long segments. The rationale behind this behavior is similar to the one described for the sensitivity of the segments density versus the compression strain in Section 6.1.

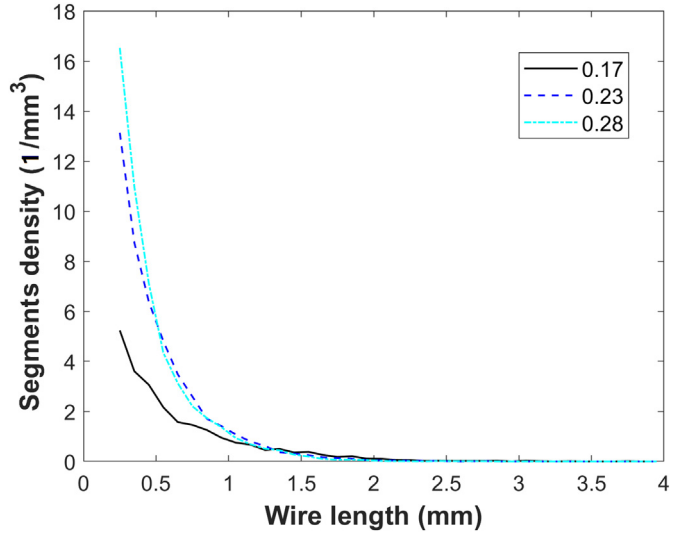

Fig. 26. Segments densities versus segments lengths with different metal rubber relative densities.

The quasi-static cyclic test results of MR samples with different relative densities are shown in Fig. 27. The evident presence of hysteretic loops indicates good energy absorption properties. The maximum compression forces provided on the three specimens are all ~95 N, even though the maximum deformations are different; this clearly denotes the presence of different stiffness values (as expected [15,23]).

The tangent moduli of the three specimens during loading are shown in Fig. 27(b). The three curves all steeply decrease first, and then slowly rise with the increasing strain. The initial reduction is caused by the transformation of the contact state between wires. The three MR specimens used here are all subjected to a 5 N compressive preload, mainly causing the wires to stick. When the compression loading of the test is applied, the MR specimen begins to deform and the stick contact state tends to transform into slip, which has a smaller stiffness [15,23]. The tangent modulus therefore declines significantly during the first portion of the curve. The internal structure of the metal rubber becomes however denser with more contact pairs and shorter wire segments when the compressing deformation increases. That implies that the number of coils n in the helix cell model of Fig. 5 is reduced by the compression load. Eq. (1) indicates that the axial and lateral stiffness of helix cell both increase monotonically with n; therefore the modulus begins to increase though the contact pairs are mostly under slip.

Fig. 27 also gives evidence to the increase of the modulus with relative density at different strains, consistent with reference [45]. The

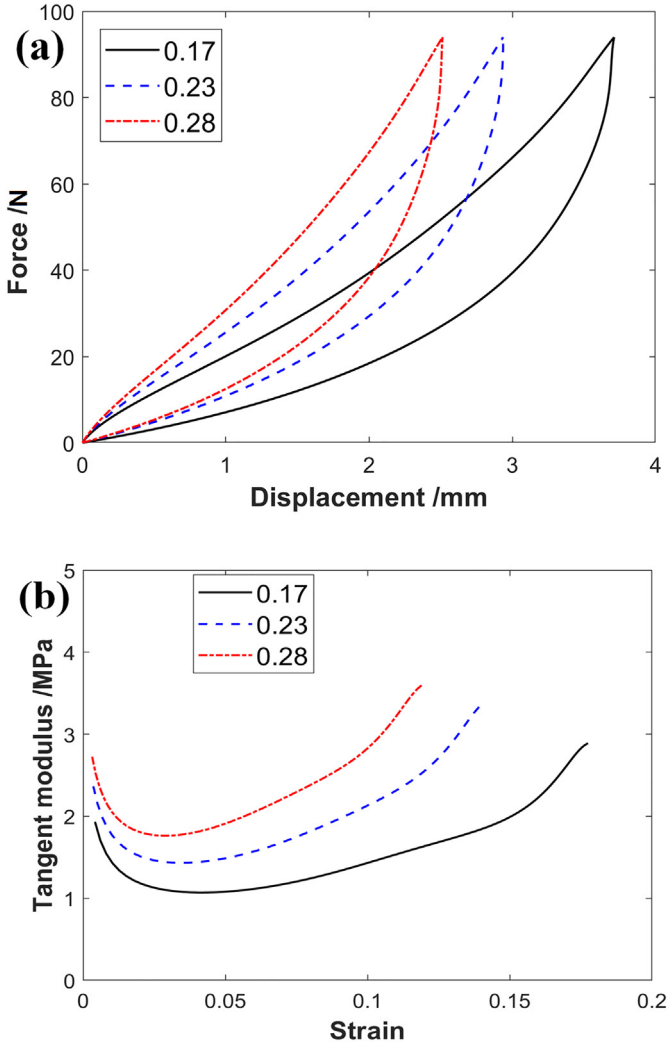

Fig. 27. Quasi-static test results of the metal rubber samples with different relative densities. (a) Hysteretic loops, (b) Tangent modulus.

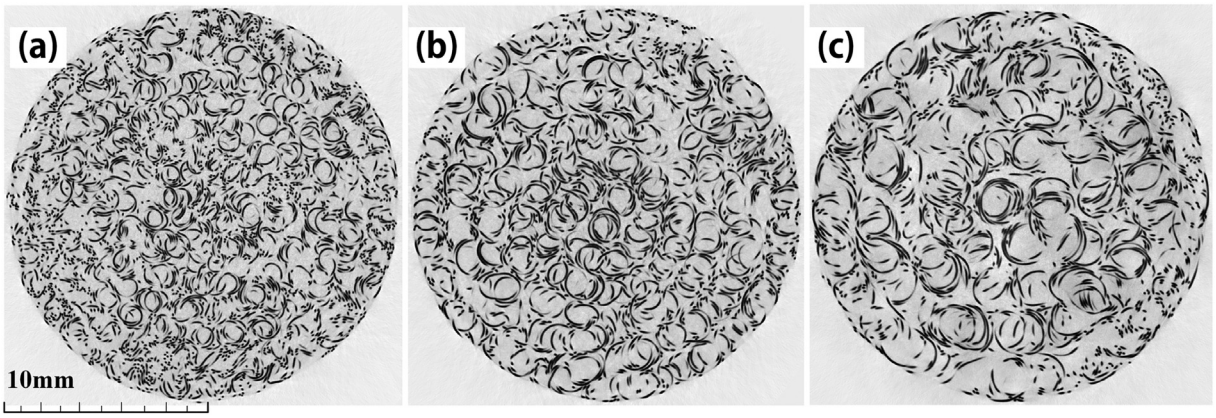

Fig. 28. Cross sections of MR specimens with different helix diameters. (a) $D_h = 1.0$ mm, (b) $D_h = 1.5$ mm, (c) $D_h = 2.0$ mm.

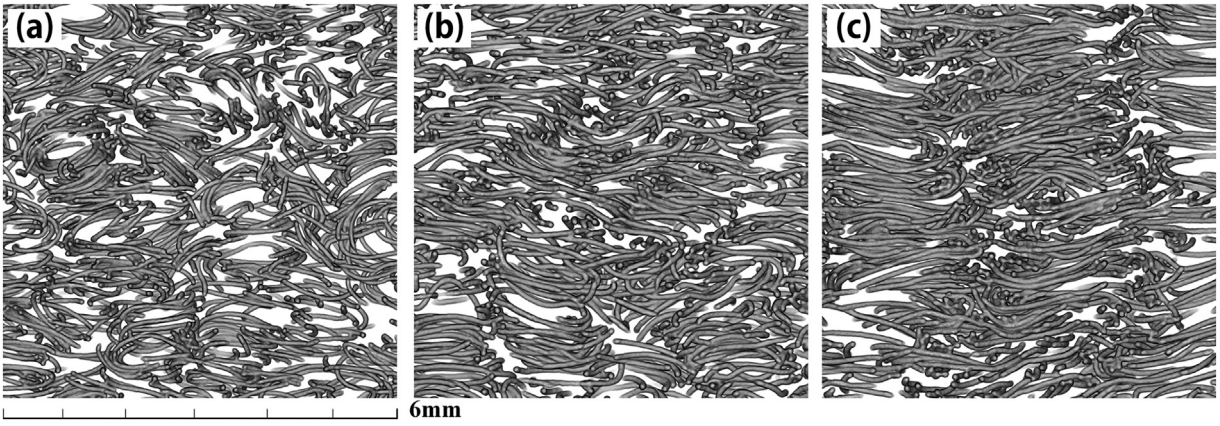

Fig. 29. Lateral slices of MR specimens with different helix diameters. (a) $D_h = 1.0$ mm, (b) $D_h = 1.5$ mm, (c) $D_h = 2.0$ mm.

modulus rises by 69.2% from 1.07 MPa to 1.81 MPa at 4% strain when ρ_r increases from 0.17 to 0.28. This is because the higher relative density results in a denser internal structure of the metal rubber with more contact pairs and shorter wire segments, which leads to the presence of smaller coil numbers of the helix cell and therefore higher stiffness.

The loss factor η of the metal rubber can be obtained from quasi-static tests and calculated by the expression $\eta = \Delta W/(2\pi U)$, where ΔW is the energy dissipated during one loading–unloading cycle, and U is the maximum energy stored during a cycle [23,46]. The loss factors of the MR samples with $\rho_r = 0.17$, 0.23 and 0.28 are 0.19, 0.18 and 0.20 respectively. These values are consistent with the ones observed in open literature [27]. There is no obvious evidence of influence caused by the relative density on the loss factor of the metal rubber.

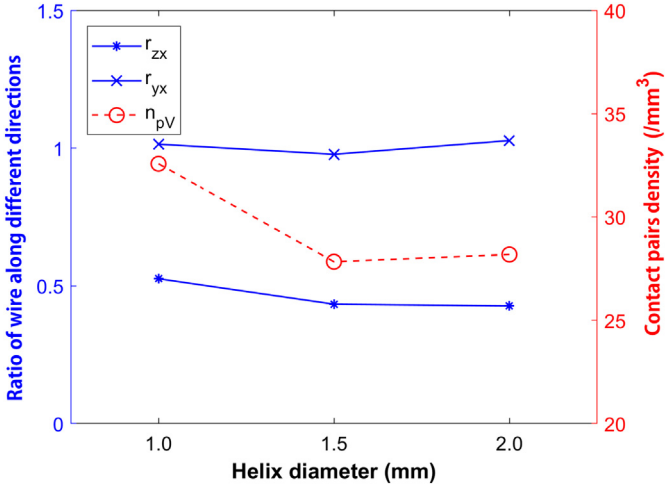

Fig. 30. Wire orientation ratios and contact pairs density versus helix diameter.

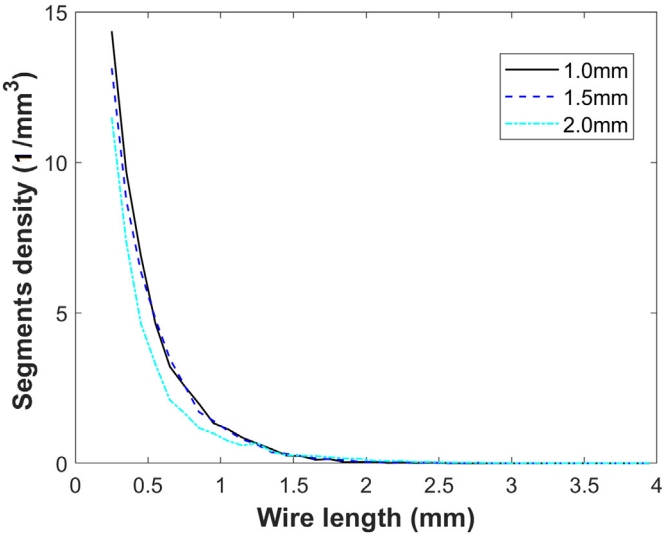

Fig. 31. Segment densities versus segment lengths with different helix diameters.

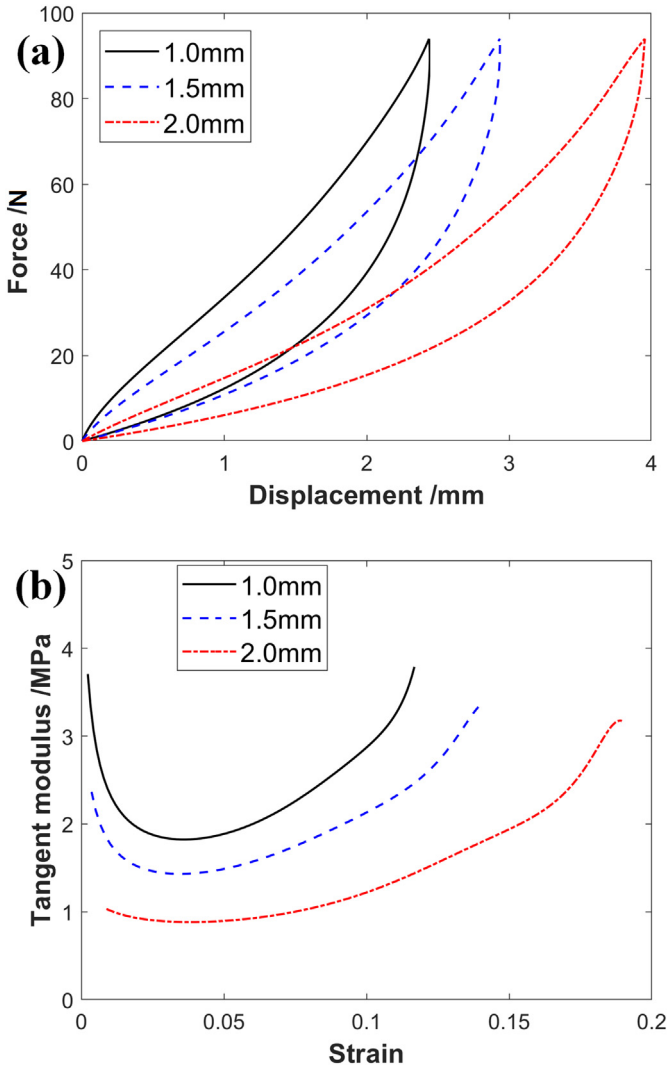

Fig. 32. Quasi-static test results of metal rubber samples with different helix diameters (a) Hysteretic loops, (b) Tangent modulus.

6.3. Variation of the helix diameter

The helix diameter D_h used for manufacturing the samples can also affect the overall mechanical properties of the metal rubber. The specimens #4–1, #2-1a and #5–1 with D_h of 1.0 mm, 1.5 mm and 2.5 mm respectively were tested and compared to investigate the potential influence of the values of helix diameter. The cross sections of the three specimens are shown in Fig. 28. The diameter of the ring-shaped wire cutting areas becomes larger when D_h increases. Besides, the percentage of point-shaped wire cutting areas decreases with increasing D_h. This is explained by the fact that more helix cells tend to distribute along the molding direction when D_h rises.

Lateral slices (sizes 6 mm × 6 mm × 1 mm) of MRs with different helix diameters are shown in Fig. 29. The wires are distributed more disorderly, and the helices are orientated along different directions when $D_h = 1.0$ mm. In contrast, when D_h increases, the wires tend to feature a more regular arrangement, with more helices oriented along the molding direction.

The curves of wire fractions per section versus specimen height for MRs with different D_h are all quite similar to the black curve shown in Fig. 7. The wire ratio r_{yx} in Fig. 30 is almost not affected by the value of D_h (the range is between 0.97 and 1.06). The wire ratio r_{zx} slightly decreases from 0.54 to 0.41 when the helix diameter increases, suggesting that a lower portion of wires tends to orient along the molding direction in MR in the case of large helix diameters; this coincides well with the results shown in Fig. 28 and Fig. 29. The contact pairs density n_{pV} however declines by 13%, from 32.6 1/mm^3 to 28.2 1/mm^3, when D_h increases from 1.0 mm to 2.0 mm. That means a lower number of contact pairs is generated by the well-ordered distribution of wires with larger D_h values.

Fig. 31 shows the comparison between segments densities for the three classes of MRs with different helix diameters. When the value of D_h reduces, the number of short segments slightly increases, while the portion of long segments in the porous solid has a small drop. For example, the segments densities are 14.4 1/mm^3 and 0.041 1/mm^3 respectively for the 0.2–0.3 mm and 1.9–2.0 mm ranges in metal rubber sample with $D_h = 1.0$ mm. This needs to be compared against the 11.5 1/mm^3 and 0.15 1/mm^3 values for MR with $D_h = 2.0$ mm. The wires are distributed into slightly longer segments on average because of a lower number of contact pairs exists in metal rubber with larger helix diameters.

The quasi-static cyclic tests of metal rubber samples with different helix diameters are shown in Fig. 32. The shape and changing trend of the three hysteretic loops and tangent modulus curves are all quite similar, however the specific values differ substantially. The modulus decreases first with increasing compressive strain, and then increases with the loading, and this is similarly to the uniaxial compression case shown in Fig. 27. The modulus increases with decreasing D_H values at different strains. For example, the tangent modulus rises by 108.0% from 0.88 MPa to 1.83 MPa, when D_H varies from 2.0 mm to 1.0 mm at 4% strain.

The rationale behind this behavior lies in the monotonic decrease of the axial and lateral stiffness of the helix cell versus increasing values of D_H (Eq. (1)). The helices also tend to mostly orient along the molding

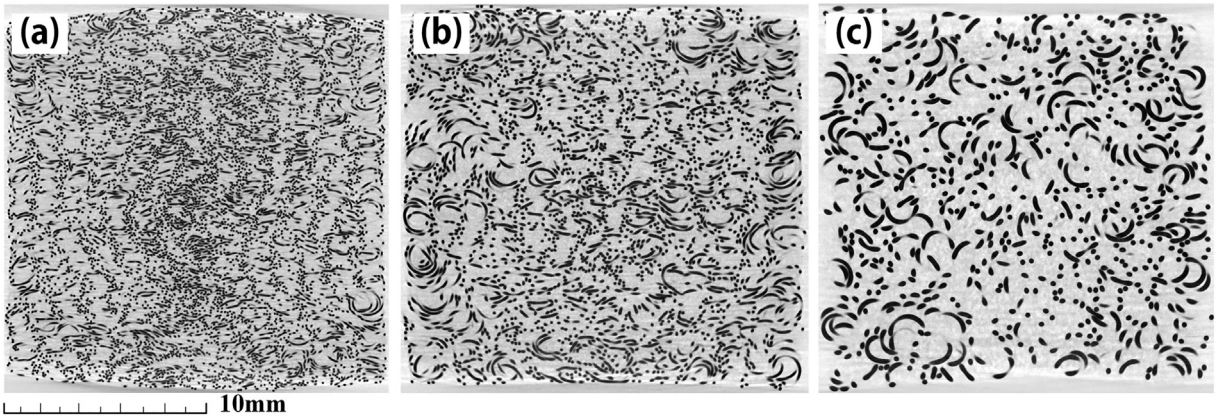

Fig. 33. Lateral sections of the MR specimens with different wire diameters: (a) $D_w = 0.08$ mm, (b) $D_w = 0.15$ mm and (c) $D_w = 0.25$ mm.

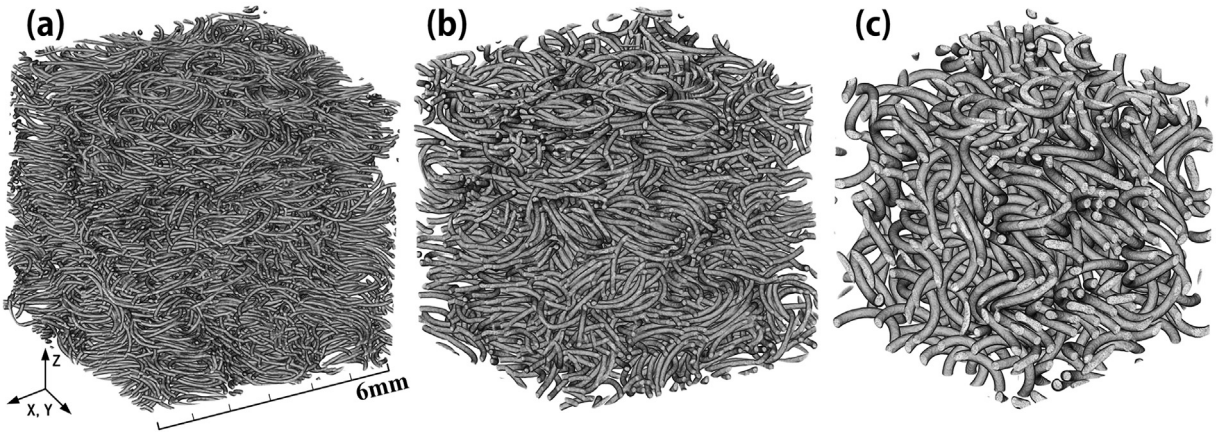

Fig. 34. 3D models of the MR specimens with different wire diameters. (a) $D_w = 0.08$ mm, (b) $D_w = 0.15$ mm, (c) $D_w = 0.25$ mm.

direction when $D_H = 2.0$ mm, different from the disorderly distribution observed when $D_H = 1.0$ mm. A further reduction of the modulus along the molding direction is therefore expected when larger helix diameters are adopted.

The loss factors of the MR samples with helix diameters of 1.0 mm, 1.5 mm and 2.0 mm are 0.22, 0.19 and 0.18, respectively. The loss factors appear to decrease only slightly when the helix diameter becomes larger. This implies that metal rubber systems with small helix diameter values possess high stiffness and, at the same time, adequate energy dissipating capability for engineering vibration applications.

6.4. Variation of the wire diameter

The diameter of the wires used to manufacture metal rubber is also an essential parameter for the mechanical characteristics. Specimens #2-1a, #6–1 and #7–1 were therefore tested and evaluated to investigate the effect of the wire diameter D_w on the structural and mechanical performances of the porous material. The lateral sections of the three metal rubber specimens are visualized in Fig. 33. The wire cutting areas become larger and sparser as the value of D_w increases. Although the relative densities are the same, the total wire length of the metal rubber with $D_w = 0.25$ mm is only 10.2% of the analogous MR material with $D_w = 0.08$ mm. Also, the percentage of ring-shaped wire cutting areas increases with D_w, and this indicates a larger number of helices oriented along the non-molding directions.

The cube samples cut out from the three metal rubbers with different D_w values are shown in Fig. 34. The cubes exhibit some obvious differences. The wires become much thicker and more sparsely distributed as D_w increases from 0.08 mm to 0.25 mm. The wire orientation also becomes more disorderly, with more wires distributed along the molding direction. Besides, the angle α of the helix cell obviously increases with larger values of D_w.

The section wire fractions of MRs with different D_w are compared in Fig. 35. The three curves are quite similar, with the evident presence of boundary layers and uniform middle parts. The thickness of the boundary layer increases slightly with D_w, which is ~0.7 mm for MR with $D_w =$ 0.08 mm compared to the case of ~1.3 mm when $D_w = 0.25$ mm.

The wire orientation ratios and contact pairs densities versus the wire diameter D_w are shown in Fig. 36. The ratio r_{yx} is almost insensitive to the variation of D_W, shifting between 0.94 and 1.04. This indicates small variations along the different non-molding directions. The ratio r_{zx} however increases significantly from 0.41 to 1.04 as D_w rises from 0.08 mm to 0.25 mm; this is a peculiar and different behavior with respect to the sensitivity of the other parameters examined above. The maps of wire orientation distribution of samples with $D_w = 0.08$ mm, 0.15 mm and 0.25 mm are shown in Fig. 11, Fig. 37(a) and Fig. 37 (b) respectively. The three maps vary significantly, from a strip distribution shape for $D_w = 0.08$ mm to a more disorderly distribution present for $D_w = 0.25$ mm. The normalized projection q_g varies from 1 to ~2.42 when $D_w = 0.08$ mm, with the maximum values at the equator and the minimum ones at the poles. In the case of the metal rubber with $D_w =$

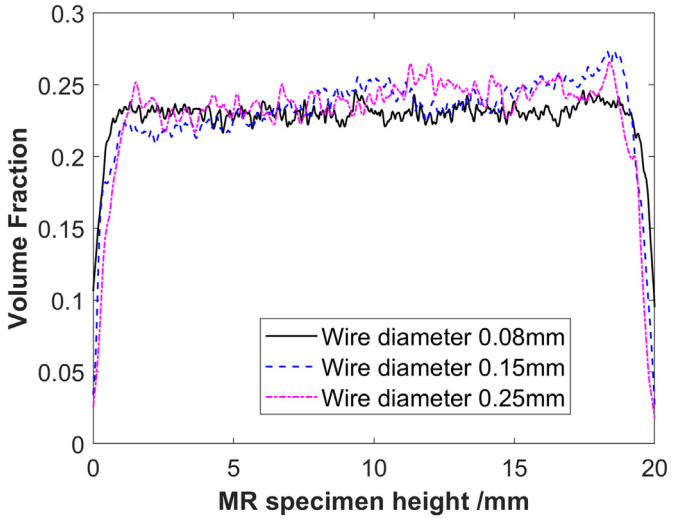

Fig. 35. Section wire fraction versus specimen height of MRs with different D_w.

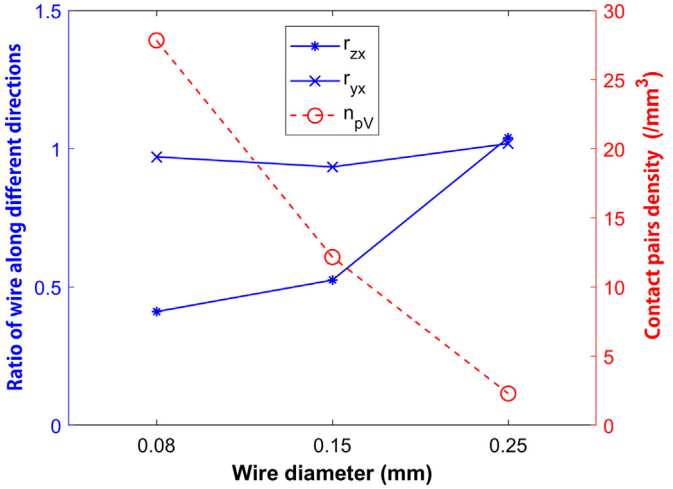

Fig. 36. Wire orientation ratios and contact pairs density versus wire diameter.

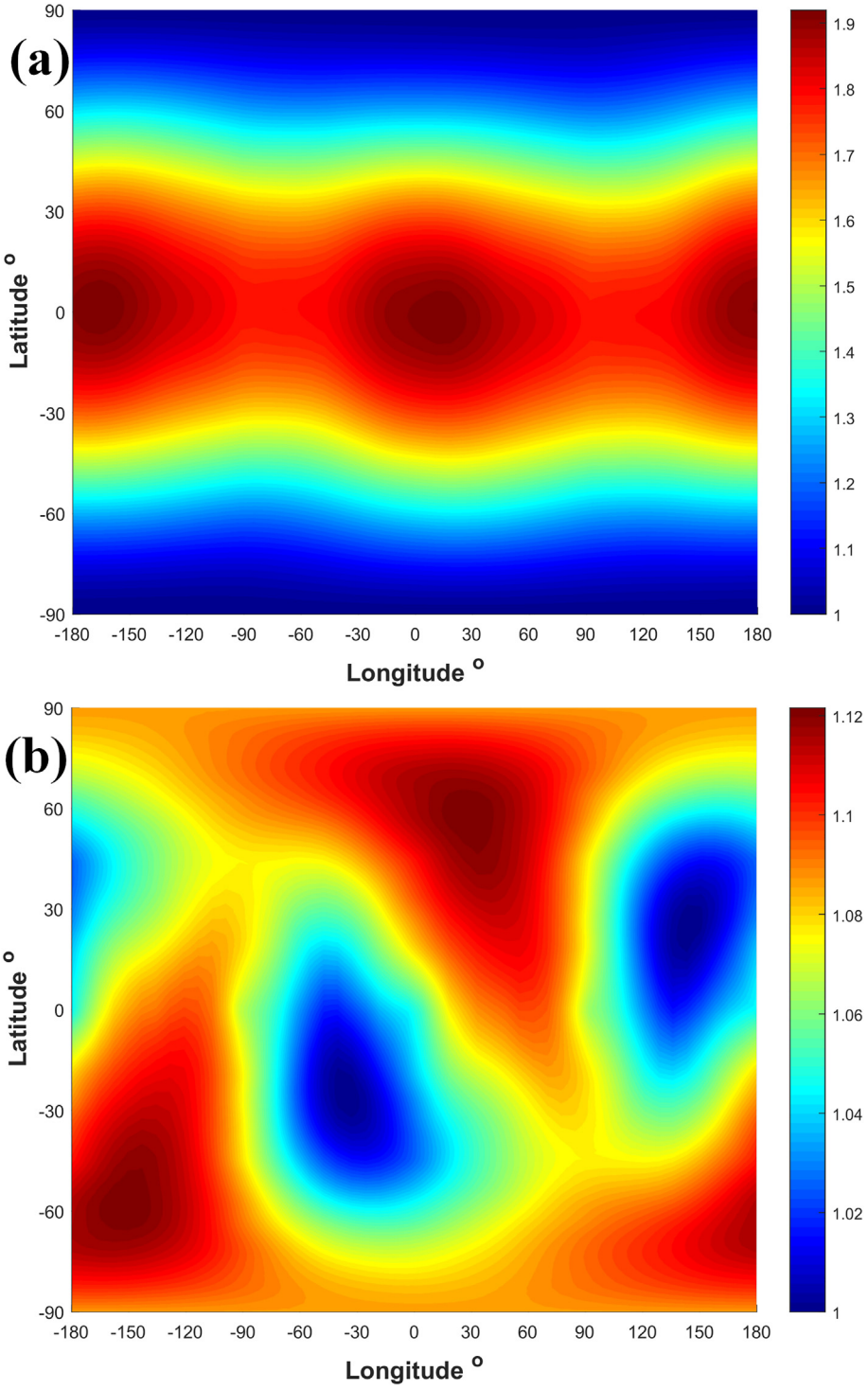

Fig. 37. Orientation distribution map of wire in MR specimens with different wire diameters (a) $D_w = 0.15$ mm, (b) $D_w = 0.25$ mm.

0.25 mm, the projection q_g ranges from 1 to ~1.12, with maximum and minimum values distributed in a random fashion. These results indicate that more wires tend to align along the molding direction and the transverse isotropy of the internal structure becomes less obvious for MRs with thicker wires. The metal rubber almost assumes the form of an isotropic material from a structural perspective when the diameter D_w becomes 0.25 mm. The contact pair density n_{pV} also decreases significantly from 27.8 1/mm^3 to 2.3 1/mm^3 when D_w increases from 0.08 mm to 0.25 mm. This indicates that the number of contact pairs is largely reduced by increasing the wire diameter D_w, as it can be readily observed from Fig. 33 and Fig. 34.

The segments density curves with different D_w values are shown and compared in Fig. 38. The histogram of the segments within different length ranges for $D_w = 0.25$ mm is also added in Fig. 38 to illustrate the curve more clearly. The three curves all decrease with the increase of the segment length, with a much steeper decline for metal rubber specimens with smaller values of D_w. The number of short segments in metal rubber samples with small D_w values is significantly higher

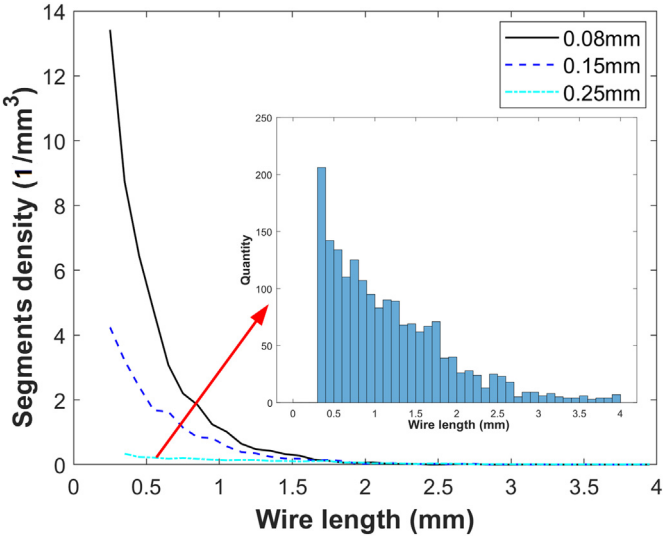

Fig. 38. Segments densities versus segments lengths in MR samples with different wire diameters.

than the one with larger D_w values, compared with the cases with smaller numbers of long segments. For example, the segment density is 8.74 1/mm^3 and 0.0068 1/mm^3 for wire lengths of 0.3–0.4 mm and 2.5–2.6 mm respectively when the metal rubber wire has a diameter of 0.08 mm. When the wire diameter is 0.25 mm the densities decrease to 0.34 1/mm^3 and 0.038 1/mm^3 for the above wire lengths ranges. This is because the metal rubber with a thick wire has a sparser distribution, with less wires and contact pairs; the single wires are therefore subdivided into longer segments by the contact pairs on average.

The results from quasi-static cyclic tests on specimens with different D_W values (the #8–1, #9–1 and #10–1 in Table.1) are shown in Fig. 39. The load was applied along the molding direction Z and non-molding directions X and Y. Only the results along the Z and X directions are shown because the difference between data along the X and Y non-molding directions is negligible. It can be seen that the stiffness along non-molding direction is much higher than the one along molding direction, consistent with reference [45]. The stiffness along the Z direction increases significantly with D_W while the stiffness along X decreases with increasing wire diameters.

The tangent modulus along the molding and non-molding directions are shown in Fig. 39(b) and (c) respectively. All curves show a similar shape, first with a decrease and then followed by an increase. The tangent modulus along the Z direction increases by 82% from 1.11 MPa to 2.02 MPa when D_W increases from 0.08 mm to 0.25 mm at a value of 3.5% strain. On the contrary, the tangent modulus along the X direction decreases by 37%, from 11.5 MPa to 7.26 MPa at 0.68% strain for the same change of D_W values.

The different stiffness in the molding and non-molding directions can be explained by the structural characteristics described in the previous paragraphs. It is easy to know from Eq. (1) that the axial and lateral stiffness of the helix cell in Fig. 5 rise monotonically for increasing wire diameters. The stiffness K_L is always larger than K_A when $\alpha < 10^\circ$ and $n < 0.5$ (Fig. 6). More helices tend to align along the non-molding direction with increasing values of D_W, and this results in the increase of the MR modulus along the molding direction, even with the presence of reduced numbers of contact pairs and segments. This also leads to a reduced modulus along the non-molding directions. The lead angle α of helix cell in Fig. 5 also increases with the wire diameter, resulting in a higher K_A/K_L ratio (Fig. 6). Thus, the modulus along the molding direction increases further, while the modulus along the non-molding direction tends to decline more.

When the wire diameter is equal to 0.08 mm, the internal structure of the metal rubber assumes a transverse isotropic behavior, with the majority of the helices oriented along molding direction. If one considers that K_A is lower than K_L for metal rubber helix cells, the modulus of the MR in the non-molding direction is larger than the one along the molding one. When $D_W = 0.25$ mm, the internal structure of the MR

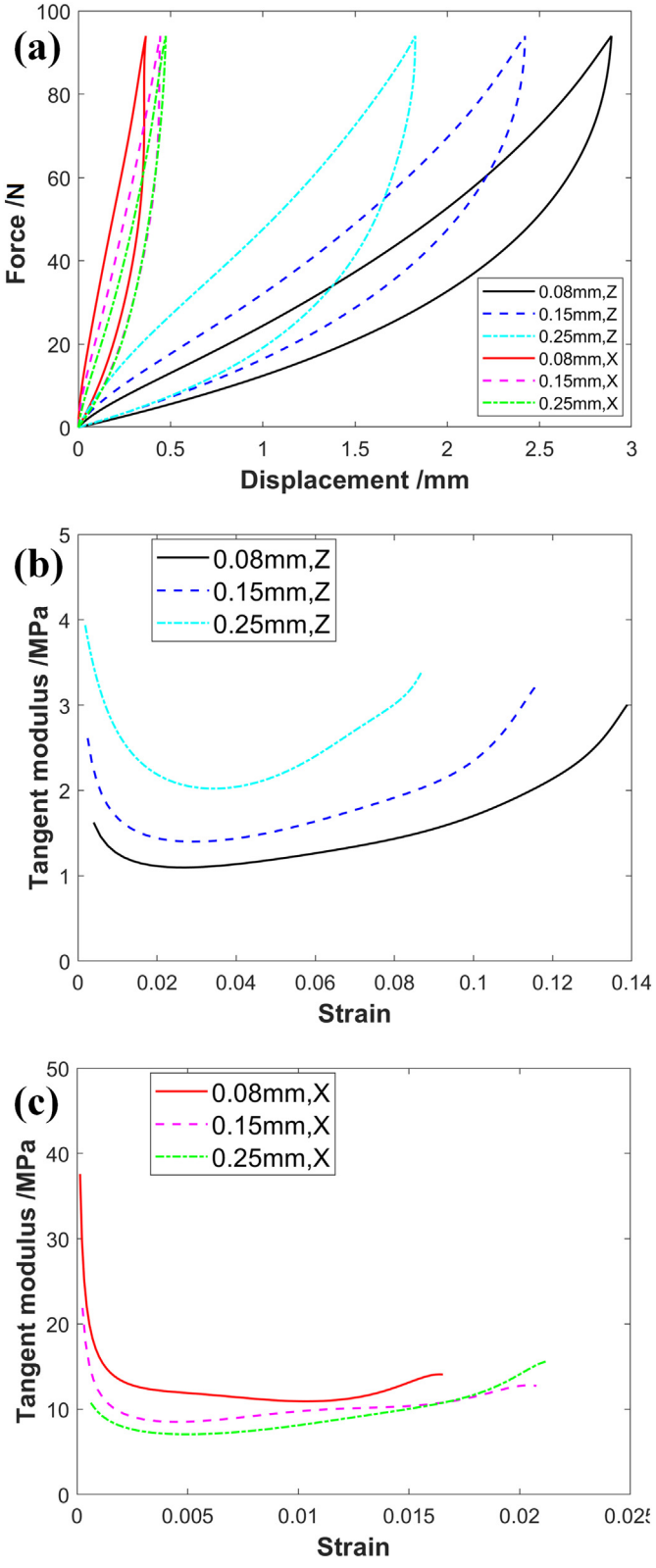

Fig. 39. Quasi-static loading of metal rubber samples with different wire diameters (a) Hysteretic loops, (b) Tangent modulus along the molding direction Z, (c) Tangent modulus along the non-molding direction X.

Table 2
Loss factors of cube MR specimens with different D_W.

D_W/mm	Loss factor along different directions		
	Z	X	Y
0.08	0.147	0.261	0.262
0.15	0.150	0.236	0.242
0.25	0.220	0.178	0.172

appears to possess an isotropic wire orientation, however the modulus along the molding and non-molding directions still exhibits large differences. The reason behind this discrepancy is the fact that during the manufacturing the MR is compressed into a significantly smaller space in the mold, and then it returns to the designed height after. This results in the initial stress state of the MR along molding direction, with the related modulus being much smaller than that of the non-molding direction.

The loss factors of the cubic MR specimens with different D_W measured along the molding and non-molding directions are compared in Table.2. The loss factor increases with D_W when the loading occurs in the molding direction, while it declines in the transverse one. The loss factors along the two non-molding directions are quite similar. The loss factor is smaller along the molding direction than the non-molding direction when the wire diameters are equal to 0.08 mm and 0.15 mm, and larger when $D_W = 0.25$ mm. It is apparent that the MR with larger D_W values has higher stiffness and vibration energy dissipating capability, and this is particularly interesting for engineering vibroacoustics applications.

The transverse isotropy of the MR loss factor is mainly caused by the configuration of the metal rubber internal topology. As observed from the CT scan results, the inner structure of the MR with smaller D_W exhibits a stack of coils along the molding direction. That means the sliding distances at contact pairs under lateral compression are significantly larger than under axial compression, resulting in a greater loss factor value along the non-molding direction for the case of metal rubber with thin wire. When D_W increases, more wires orient along the molding direction and the structural transverse isotropy of the metal rubber becomes less obvious. Therefore, the loss factor measured when loading along the molding direction increases, while the one along the non-molding direction decreases. Although the wire orientation exhibits isotropy when $D_W = 0.25$ mm, the modulus along the molding direction is much smaller than the one along the non-molding direction because of the initial stress state inside the MR, as discussed above. Therefore, the MR specimens tend to exhibit larger deformations under axial compression, with the contact pairs sliding at further distance. This results in higher loss factors along the Z direction.

7. Conclusions

In this work the microscopic structural characteristics of metal rubber (entangled wire) materials has been evaluated using CT scans and skeletonisation methods. These approaches and techniques used in this paper have allowed the identification of metrics to statistically describe the topology of MR. The mechanical properties of metal rubber have been evaluated by quasi-static tests. It is shown that the metal rubber exhibits obvious transverse isotropy along the different directions. The effect of the different parameters on the mechanical properties of metal rubber has been introduced here and explained by combining a simplified helix cell model and the results from the tests on the internal MR structure. It is found that the wire diameter has the most significant effect on both the mechanical properties and the structural (topological) characteristics of the metal rubber. The information contained in this work provides a coherent picture of the detailed internal microstructure of metal rubber, and provides insights on how to improve the manufacturing process by highlighting the fundamental metrics that underpin the overall mechanical behavior of this interesting porous metal material.

Credit author statement

Yanhong Ma: Acquired and lead the funding project. Provided the conceptualization and methodology of the research. Gave some guidance and help on the methodology and result analysis, including theory and experiments.

Qicheng Zhang: Finished the CT scan tests and quasi-static tests. Processed the experimental data and finished the manuscript.

Yongfeng Wang: Did work on the skeleton model extraction from the 3D model of metal rubber. Assisted on the experiment of CT scan and quasi-static test.

Jie Hong: Acquired and lead the project. Give some help and supervision on the research conceptualization, data analysis and theoretical model.

Fabrizio Scarpa: Gave helpful suggestion and guidance on the research idea and methodology. Helped revising the manuscript thoroughly.

Acknowledgement

The authors thank the National Natural Science Foundation of China for the funding (Grant numbers: 11672017 and 51475023). FS acknowledges the support of the University of Bristol for the research activity.

References

[1] P. Liu, G. He, L. Wu, Uniaxial tensile stress–strain behavior of entangled steel wire material[J], Materials Science & Engineering A 509 (1) (2009) 69–75.
[2] G. He, P. Liu, Q. Tan, Porous titanium materials with entangled wire structure for load-bearing biomedical applications.[J], J. Mech. Behav. Biomed. Mater. 5 (1) (2012) 16–31.
[3] M. Zarzour, J. Vance, Experimental Evaluation of a Metal Mesh Bearing Damper[J], Journal of Engineering for Gas Turbines & Power 122 (2) (2000) 326–329.
[4] B.H. Ertas, H. Luo, Nonlinear Dynamic Characterization of Oil-Free Wire Mesh Dampers[J], Journal of Engineering for Gas Turbines & Power 130 (3) (2007) 1225–1234.
[5] B. Ertas, H. Luo, D. Hallman, Dynamic characteristics of shape memory alloy metal mesh dampers[C], 50th AIAA/ASME/ASCE/AHS/ASC Structures, Structural Dynamics, and Materials Conference 17th AIAA/ASME/AHS Adaptive Structures Conference 11th AIAA no 2009, p. 2521.
[6] S. Li, C. Mao, H. Li, et al., Mechanical properties and theoretical modeling of self-centering shape memory alloy pseudo-rubber[J], Smart Materials & Structures 20 (11) (2011) 271–278.
[7] Y. Ma, Q. Zhang, Y. Dobah, et al., Meta-tensegrity: Design of a tensegrity prism with metal rubber[J], Compos. Struct. 206 (2018) 644–657.
[8] Q. Zhang, D. Zhang, Y. Dobah, et al., Tensegrity cell mechanical metamaterial with metal rubber[J], Appl. Phys. Lett. 113 (3) (2018) 031906.
[9] K. Xiao, H. Bai, X. Xue, et al., Damping characteristics of metal rubber in the pipeline coating system[j], Shock. Vib. 2018 (2018) 1–11 (Volume, Article ID 3974381).
[10] B. Ertas, E. Al-Khateeb, J. Vance, Cryogenic temperature effects on metal mesh dampers and liquid hydrogen turbopump rotordynamics, 38th AIAA/ASME/SAE/ASEE Joint Propulsion Conference & Exhibit 2002, p. 4164.
[11] M. Zarzour, J. Vance, Experimental evaluation of a metal mesh bearing damper, J Eng Gas Turbines Power-Trans ASME 122 (2) (2000) 326–329.
[12] Y. Ma, Q. Zhang, D. Zhang, F. Scarpa, B. Liu, J. Hong, Tuning the vibration of a rotor with shape memory alloy metal rubber supports, J Sound Vibr 351 (2015) 1–16.
[13] M. Rannenberg, H. Beer, Heat transfer by evaporation in capillary porous wire mesh structures[J], Letters in Heat & Mass Transfer 7 (6) (1980) 425–436.
[14] G. He, P. Liu, Q. Tan, Porous titanium materials with entangled wire structure for load-bearing biomedical applications.[J], J. Mech. Behav. Biomed. Mater. 5 (1) (2012) 16–31.
[15] Y. Ma, Q. Zhang, D. Zhang, F. Scarpa, B. Liu, J. Hong, The mechanics of shape memory alloy metal rubber, Acta Mater. 96 (2015) 89–100.
[16] Y. Ma, Q. Zhang, D. Zhang, F. Scarpa, B. Liu, J. Hong, A novel smart rotor support with shape memory alloy metal rubber for high temperatures and variable amplitude vibrations, Smart Mater. Struct. 23 (12) (2014), 125016.
[17] B. Gadot, O.R. Martinez, S.R.D. Roscoat, et al., Entangled single-wire NiTi material: A porous metal with tunable superelastic and shape memory properties[J], Acta Mater. 96 (2015) 311–323.
[18] Y. Ma, Q. Zhang, D. Zhang, et al., Tuning the vibration of a rotor with shape memory alloy metal rubber supports[J], J. Sound Vib. 351 (2015).
[19] Y. Ma, Q. Zhang, D. Zhang, W. Hu, J. Hong, Experimental investigation on the dynamic mechanical properties of soft magnetic entangled metallic wire material, Smart Mater. Struct. 26 (5) (2017), 055019.

[20] Y. Ma, W. Hu, D. Zhang, Q. Zhang, J. Hong, Tunable mechanical characteristics of a novel soft magnetic entangled metallic wire material, Smart Mater. Struct. 25 (9) (2016), 095015.
[21] G. He, Q. Tan, G. Jiang, et al., A novel mechanism for auxetic behavior in entangled materials with a spiral wire structure[J], Smart Materials & Structures 23 (9) (2014), 095011.
[22] H. Zuo, Y.H. Chen, H.B. Bai, et al., The Compression Deformation Mechanism of a Metallic Rubber[J], International Journal of Mechanics & Materials in Design 2 (3-4) (2005) 269–277.
[23] D. Zhang, F. Scarpa, Y. Ma, et al., Compression mechanics of nickel-based superalloy metal rubber[J], Materials Science & Engineering A 580 (37) (2013) 305–312.
[24] J. Hu, Q. Du, J. Gao, et al., Compressive mechanical behavior of multiple wire metal rubber[J], Mater. Des. 140 (2018) 231–240.
[25] Y. Ma, Q. Zhang, D. Zhang, et al., Size-dependent mechanical behavior and boundary layer effects in entangled metallic wire material systems[J], J. Mater. Sci. 52 (7) (2017) 3741–3756.
[26] Y. Ma, H. Wang, H. Li, et al., Study on metal rubber material's characteristics of damping and sound absorption[C]//ASME Turbo Expo 2008: power for land, sea, and air, Am. Soc. Mech. Eng. (2008) 477–486.
[27] H. Wang, J.A. Rongong, G.R. Tomlinson, et al., Nonlinear static and dynamic properties of metal rubber dampers[J], energy 10 (1) (2010).
[28] Tan Qingbiao, et al., Mechanical behaviors of quasi-ordered entangled aluminum alloy wire material, Mater. Sci. Eng. A 527 (1) (2009) 38–44.
[29] P. Liu, Q. Tan, L. Wu, et al., Compressive and pseudo-elastic hysteresis behavior of entangled titanium wire mats[J], Mater. Sci. Eng. A 527 (15) (2010) 3301–3309.
[30] G. He, P. Liu, Q. Tan, et al., Flexural and compressive mechanical behaviors of the porous titanium materials with entangled wire structure at different sintering conditions for load-bearing biomedical applications.[J], J. Mech. Behav. Biomed. Mater. 28 (28C) (2013) 309–319.
[31] P. Liu, G. He, L. Wu, Uniaxial tensile stress–strain behavior of entangled steel wire material[J], Materials Science & Engineering A 509 (1) (2009) 69–75.
[32] Q. Tan, G. He, Stretching behaviors of entangled materials with spiral wire structure [J], Mater. Des. 46 (4) (2013) 61–65.
[33] P. Liu, G. He, L. Wu, Structure deformation and failure of sintered steel wire mesh under torsion loading[J], Mater. Des. 30 (6) (2009) 2264–2268.
[34] D. Zhang, F. Scarpa, Y. Ma, et al., Dynamic mechanical behavior of nickel-based superalloy metal rubber[J], Mater. Des. 56 (4) (2014) 69–77.
[35] D. Rodney, B. Gadot, O.R. Martinez, et al., Reversible dilatancy in entangled single-wire materials[J], Nat. Mater. 15 (1) (2016) 72.
[36] Y. Li, X. Huang, W. Mao, A theoretical model and experimental investigation of a nonlinear constitutive equation for elastic porous metal rubbers, Mech. Compos. Mater. 41 (4) (2005) 303–312.
[37] W. Peng, H. Bai, J. Zheng, X. Tang, et al., A Micromechanics Constitutive Model of the Metal Rubber Materials Based on the Radial and Axial Combined Deformation of the Microsprings, J Exp Mech 3 (2005) 021.
[38] B. Guo, Z. Zhu, R. Cui, Theoretical model of metal rubber, Journal of Aerospace Power 19 (2004) 314–319.
[39] J. Hong, B. Zhu, Y. Ma, Theoretical and Experimental Investigation on Nonlinear Characterization of Metal Rubber, Proceedings of ASME TURBO EXPO, Vancouver, Canada, June 6-10 2011, p. 45772.
[40] Y. Ma, Q. Zhang, D. Zhang, et al., The mechanics of shape memory alloy metal rubber [J], Acta Mater. 96 (2015) 89–100.
[41] J.C. Tan, J.A. Elliott, T.W. Clyne, Analysis of tomography images of bonded fibre networks to measure distributions of fibre segment length and fibre orientation[J], Adv. Eng. Mater. 8 (6) (2006) 495–500.
[42] J.P. Masse, C. Barbier, L. Salvo, et al., Mechanical and structural characterization of nonsintered and sintered steel wools by x-ray tomography: Description of the techniques and validation on virtual materials[J], J. Mater. Res. 28 (20) (2013) 2852–2860.
[43] Q. Wang, X. Huang, W. Zhou, et al., Three-dimensional reconstruction and morphologic characteristics of porous metal fiber sintered sheet[J], Mater. Charact. 86 (8) (2013) 49–58.
[44] X. Huang, Q. Wang, W. Zhou, et al., A simple fracture energy prediction method for fiber network based on its morphological features extracted by X-ray tomography [J], Mater. Sci. Eng. A 585 (2013) 297–303.
[45] Ren Z, Chen Q, Bai H, et al. Study on damping energy dissipation characteristics of cylindrical metal rubber in nonforming direction[J]. Adv. Mater. Sci. Eng.. 2018, ID 5014789,1–10.
[46] H. Cheng, F. Scarpa, T. Panzera, et al., Shear stiffness and energy absorption of auxetic open cell foams as sandwich cores[J], Phys. Status Solidi B 256 (1) (2019), 1800411.